Nano Research

ISSN 1998-0124 CN 11-5974/O4
https://doi.org/10.26599/NR.2026.94908632

Sulfur/oxygen vacancy synergistic engineering in MoS_2-based neuromorphic devices

Pan Pan[1,2], Ruixiao Ou[1,2], Xiaolong Fan[1], Jianxian He[1], Siyi Wu[1], Chaogui Huang[1], Hasimuali Kanikai[1], Meila Peng[1], Xu Li[1], Javed Iqbal Saggu[3], Ming Xiao[1,2](✉)

[1] School of Microelectronics Science and Technology, Sun Yat-sen University, Zhuhai 519082, China

[2] Zhuhai Key Laboratory of Nano Sensing and Intelligent Detection, Zhuhai 519082, China

[3] Department of Physics, Quaid I Azam University, Islamabad 45320, Pakistan

Nano Res., **Just Accepted Manuscript** • https://doi.org/10.26599/NR.2026.94908632

https://www.sciopen.com/journal/1998-0124 on Mar. 11, 2026

© The Authors(s)

Just Accepted

This is a "Just Accepted" manuscript, which has been examined by the peer-review process and has been accepted for publication. A "Just Accepted" manuscript is published online shortly after its acceptance,which is prior to technical editing and formatting and author proofing. Tsinghua University Press (TUP) provides "Just Accepted" as an optional and free service which allows authors to make their results available to the research community as soon as possible after acceptance. After a manuscript has been technically edited and formatted, and the page proofs have been corrected, it will be removed from the "Just Accepted" web site and published officially with volume and article number (e.g., *Nano Research*, **2025**, *18*, 94906990). Please note that technical editing may introduce minor changes to the manuscript text and/or graphics which may affect the content, and all legal disclaimers that apply to the journal pertain. In no event shall TUP be held responsible for errors or consequences arising from the use of any information contained in these "Just Accepted" manuscripts. To cite this anuscript please use its Digital Object Identifier (DOI®),which is identical for all formats of publication.

Just Accepted

TABLE OF CONTENTS (TOC)

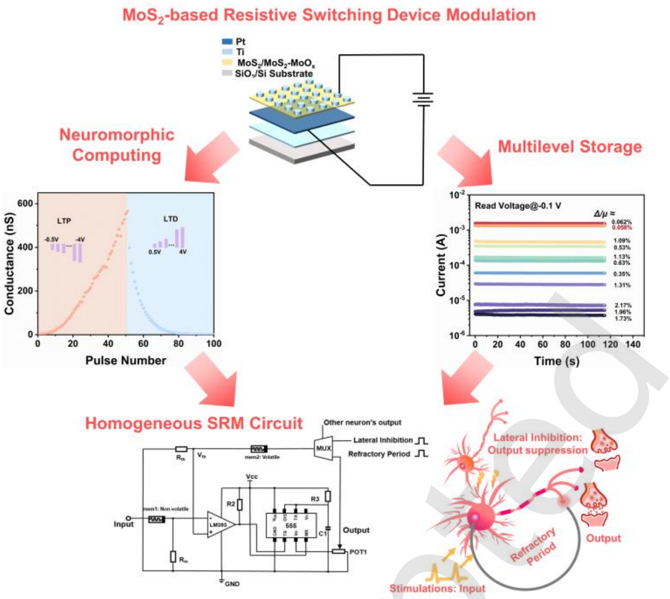

This study proposes an engineering strategy for MoS$_2$-based devices via sulfur/oxygen vacancy synergy, enabling transition from filament nonvolatile to interface-dominant volatile and filament-interface hybrid non-volatile characteristics, suitable for neuromorphic computing and multilevel storage. A homogeneous integrated spike-response model circuit involving various types of devices for refractory period/lateral inhibition emulation is designed, promising for high-accuracy recognition systems in neural network architecture.

Nano Research

Open Access

Research Article

Sulfur/oxygen vacancy synergistic engineering in MoS_2-based neuromorphic devices

Pan Pan[1,2], Ruixiao Ou[1,2], Xiaolong Fan[1], Jianxian He[1], Siyi Wu[1], Chaogui Huang[1], Hasimuali Kanikai[1], Meila Peng[1], Xu Li[1], Javed Iqbal Saggu[3], and Ming Xiao[1,2,]✉
[1]*School of Microelectronics Science and Technology, Sun Yat-sen University, Zhuhai 519082, China*
[2]*Zhuhai Key Laboratory of Nano Sensing and Intelligent Detection, Zhuhai 519082, China*
[3]*Department of Physics, Quaid I Azam University, Islamabad 45320, Pakistan*

Received: 20 January 2026; **Revised:** 9 March 2026; **Accepted:** 11 March 2026

✉Address correspondence to xiaom37@mail.sysu.edu.cn

Cite this article: *Nano Research*, 2026, 19, 94908632 https://doi.org/10.26599/NR.2026.94908632

ABSTRACT: Two-dimensional materials, especially transition metal dichalcogenides like MoS_2, show great promise for neuromorphic computing due to their highly tunable electronic properties. However, the role of defects such as sulfur vacancies (V_S), oxygen vacancies (V_O), and other in-plane defects in device operation mechanisms remains poorly understood, limiting performance and integration potential. In this work, we leverage a competitive-synergistic model of these defects to modulate resistive switching modes in MoS_2-based neuromorphic devices, transitioning from filamentary non-volatile to interface-dominated volatile and hybrid regimes. Our interface-type devices demonstrate exceptional endurance ($>10^5$ pulses) and large synaptic weight modulation range up to $>10^3$, while hybrid-type devices achieve stable multilevel states with a low variation of each state down to 10^{-4}). The transition of switching mechanism is attributed to the relative concentration of defects in MoS_2 through defect engineering protocol, which changes the dominant type of vacancy for migration. More importantly, we integrate volatile and non-volatile MoS_2 devices into a spike-response model circuit that emulates different stimulation modes and more advanced neuronal functions. This work establishes a defect engineering strategy for designing both high-performance neuromorphic and memory devices, enabling homogeneous integration for complex neural network applications.

KEYWORDS: sulfur/oxygen vacancy, synergistic defect engineering, neuromorphic devices, homogenous integration

1 Introduction

Brain-inspired artificial intelligence (AI) and neural network computing demand massive computational power[1, 2], but von Neumann architecture-based chips suffer critical inefficiency in AI and Internet of Things (IoT) tasks due to the memory-processor data transfer bottleneck[3]. To address this issue, neuromorphic chips implementing in-memory computing offer a promising solution[4]. Meanwhile, the ability of neuromorphic devices—the fundamental units within neural network computing chips—to accurately emulate synaptic properties is crucial for achieving high efficiency and accuracy in IoT tasks and AI deep learning[5]. Two-dimensional (2D) materials, featuring layered stacking based on van der Waals forces, have gained extensive application in the development of neuromorphic devices due to their efficient electron transport properties and multifunctionality[6]. Among these materials, transition metal dichalcogenides (TMDs) have garnered particular attention due to their rich defect engineering potential (primarily involving S/Se/Te vacancies) and band structure engineering[7-9]. which could reconfigure the in-plane charge distribution and accumulation characteristics. This enables more ordered vacancy migration, yielding neuromorphic devices with improved switching dynamics stability[10-12]. Furthermore, advances in low-temperature processing now enable wafer-scale integration of TMD-based integrated chips, such as the realization of medium-scale clock circuits[13], analog-to-digital converters (ADC)/digital-to-analog converters (DAC) with up to 8-bit resolution[14], and reduced instruction set computer-V (RISC-V) microprocessors[15]. This versatility in modulation strategies for realizing high-performance TMD neuromorphic devices, combined with evolving integration technologies, underscores their significant potential for hardware neural network implementations. However, the relationships among device physics, modulation approaches, and functional characteristics of these TMD materials remain inadequately elucidated[16]. Prior studies often oversimplify these complex interactions by attributing them to a single factor. Taking widely studied MoS_2 as an example, resistive switching devices employing inert metal electrodes are often attributed to sulfur vacancy (V_S) migration, while neglecting critical contributions from oxygen-related defects, molybdenum-related defects, and inter-layer grain boundary defects. In fact, oxygen ions and vacancies (V_O) within the MoS_2 lattice exert a passivation effect on V_S[17], whereas molybdenum vacancies and inter-layer grain boundary defects (particularly in multilayer MoS_2 structures)—demonstrate V_S adsorbing behavior[18]. These competing mechanisms collectively determine the overall resistive switching characteristics of MoS_2. It should be noted that the inherent sensitivity of MoS_2 to ambient H_2O and O_2[19] could lead to the formation of oxygen-incorporated MoS_2 ($MoS_{2-x}O_x$) with grain boundary defects and more V_O. This effect will compete with the intrinsic V_S-mediated conductive filament behavior. On the other hand, V_O with an increased in-plane defect density could also exhibit conductive filament formation characteristics analogous to those of intrinsic Vs[20, 21]. Additionally, sparse molybdenum vacancies introduce defect states that trigger localized charge redistribution[22], which could trap both V_O and V_S, thereby modulating the resistive switching window. Therefore, simply attributing to a single switching mechanism leads to a paradoxical phenomenon: identical mechanistic assumptions and similar modulation approaches yielding devices with different switching modes (filament-dominated vs. interface-dominated)[23-25]. This ambiguity critically compromises the correlation between the electrical characteristics of MoS_2-based resistive switching devices and their modulation strategies, such as the limited dynamic conductance ranges and insufficient endurance. Furthermore, at the neuromorphic computing level, these misunderstandings limit performance, including dynamic conductance range and endurance in neural networks (ANNs), degrading recognition accuracy for high-complexity datasets[26]. Therefore, it is imperative to incorporate oxygen defects and inter-layer defects (e.g., metal vacancies, antisite defects) into comprehensive mechanistic frameworks in TMD-based resistive devices.

In this work, by regulating sulfur vacancies, oxygen vacancies, and other in-plane defect ratios through defect engineering protocol, we achieved the transition of the resistive switching mechanism in MoS_2-based resistive switching devices—from non-volatile to volatile, and finally non-volatile. We realized these transitions via natural oxidation and oxygen plasma processing. Subsequent exposure of MoS_2 dispersions to H_2O/O_2 environments yielded interface-oxidized $MoS_{2-x}O_x$ (or MoS_2-MoO_x hybrids). Resistive devices fabricated from $MoS_{2-x}O_x$ exhibited analog *I-V* characteristics, different from the pristine filament-controlled nonvolatile MoS_2-based devices. The MoS_2-MoO_x device exhibits excellent synaptic weight update characteristics and a broad dynamic weight range, demonstrating strong potential for neural network computing applications. On the other hand, oxygen plasma bombardment of $MoS_{2-x}O_x$ introduced additional sulfur vacancies while promoting MoO_x as an oxygen reservoir. The corresponding devices demonstrated hybrid filament-interface switching characteristics and multilevel storage behavior. We found that the synergistic and competitive interactions among sulfur vacancies, oxygen vacancies, and other in-plane defects contribute to this mechanism transition. By integrating volatile and non-volatile devices sharing an identical MoS_2-MoO_x switching layer, we constructed a spike-response model (SRM) circuit to emulate different neuron transmission behaviors and spikes. This implementation successfully achieves different stimulation modes in neurons and emulates neuronal refractory periods and lateral inhibition functions, which are expected to enhance learning efficiency and recognition accuracy in spiking neural networks (SNNs). This integrated framework presents a promising solution for real-time speech processing systems. Our study establishes intrinsic correlations between defect modulation and device performance in MoS_2, while the controllable switching mechanism transformation enables monolithic and homogeneous integration of TMD-based resistive devices for complex neuromorphic scenarios.

2 Experimental

2.1 Fabrication and Electrical Characterization

Ti and Pt were sequentially deposited onto Si/SiO_2 substrates using a magnetron sputtering system (PD-500C, Wuhan PDVACUUM Technologies, China). The deposited Ti layer had a thickness of approximately 10-15 nm, followed by a Pt layer of approximately 30-50 nm. Subsequently, a dispersion of ultrasonically exfoliated MoS_2 nanoflakes in a mixed solvent of water and ethanol was then sprayed onto the Pt/Ti-coated silicon substrates using a 0.5 mm nozzle (The film thickness is approximately 50 nm, characterized by step profiler, Alpha Step). For samples requiring oxygen plasma treatment, they were placed within the chamber of a plasma cleaner (CPC-E, Chengde CIF instruments Co., ltd, China). The treatment parameters were set to an O_2 flow rate of 0.8 Pa, a power of 200 W, and processing times of 10, 20, and 30 minutes, respectively. Following photolithography, Ti, approximately 200 nm thick, was deposited using an electron-beam evaporation system (PD-450, Wuhan PDVACUUM Technologies, China). Lift-off processing was then performed to define the top electrodes.

Electrical characterization of the fabricated devices, including *I-V*, retention, endurance, STM, LTM, and LTP/LTD, was conducted using a Keysight B2912A source measure unit, and all voltage pulses were set to a fixed duration of 25 ms. The scheme of testing was described in the main text. For the SRM neuronal circuit, the circuit components utilized a comparator (LM393), a timer (NE555), a multiplexer (74HC4051), a potentiometer, and fixed resistors R_m (500 Ω) and R_{th} (1 MΩ). The specific circuit configuration is detailed in **Fig. 6(a)** in the main text. A RIGOL DP831A digital source meter, connected to the V_{cc} terminal, supplied a 5V DC bias voltage to the circuit. Input waveforms were generated using a RIGOL DG4202 function generator connected to the input terminal. Lateral inhibition signals were emulated via a RIGOL DG1022 function generator connected to one input channel of the MUX. Voltage waveforms at the V_{in}, V_{mem1}, V_{out}, V_{th}, and lateral inhibition terminals (V_{ext}) were simultaneously monitored using a RIGOL MSO5104 digital oscilloscope.

2.2 Neural Networks Simulation

A fully-connected neural network architecture comprising four layers was employed. The input image data was preprocessed into normalized grayscale pixel arrays, serving as the input layer (8×8 for small MNIST, 28×28 for both MNIST and Fashion MNIST). The input layer consisted of 784 neurons, followed by a hidden layer with 300 neurons and a fully-connected layer with 100 neurons. The output layer contained 10 neurons. Sigmoid and Softmax activation functions were applied to the hidden layer and output layer, respectively. Optimization utilized the Stochastic Gradient Descent (SGD) algorithm with a learning rate of 0.0025 over 75 training epochs.

2.3 Materials Characterization

The Raman spectra of the MoS_2 (MoS_2-MoO_x) films were acquired using a Raman imaging microscope (Renishaw, inVia) with an excitation wavelength of 532 nm. Optical absorption spectra of the films were recorded using a UV-vis-NIR spectrophotometer (SHIMADZU, UV-3600i Plus), scanning across a wavelength range of 1200 to 200 nm at a scan rate of

0.5 nm/s. XRD patterns were obtained using an X-ray diffractometer (PANalytical, Empyrean) with Cu Kα radiation, and the grazing incidence angle was set to 0.5° with the diffraction angle (2θ) ranging from 10° to 70°. XPS spectra of the S, Mo, and O elements within the films were acquired using an X-ray photoelectron spectrometer (Thermo Fisher Scientific, ESCALAB Qxi). Field-emission transmission electron microscopy (FETEM, JEM-F200 equipped with a Gatan GIF Continuum 1065 spectrometer) was employed to acquire lattice images and elemental distribution maps (S, O, Mo) for Pristine MoS_2 (P-MoS_2), naturally-oxidized MoS_2 (O-MoS_2), and O_2 plasma-treated MoS_2 (Plasma-MoS_2) samples, using an accelerating voltage of 200 keV.

Result and discussion

To investigate the influence of modulated interactions among V_O, V_S, and defects on MoS_2-based device performance, we designed the research framework outlined in **Fig. 1**. Initially, pristine MoS_2 was characterized to establish baseline resistive switching properties, confirming V_S-dominated filamentary switching behavior. Subsequently, MoS_2 nanosheet dispersions were exposed to H_2O/O_2-enriched environment to passivate intrinsic V_S while increasing oxygen ion and V_O concentrations. Ultimately, oxygen plasma bombardment was applied to oxidized MoS_2 to enhance concentrations of in-plane V_S and other types of defects. To validate the natural oxidation approach, supplementary annealing of pristine MoS_2 nanosheets under ambient atmosphere was performed to accelerate oxidation kinetics. A competitive/synergistic interplay among V_S and V_O in MoS_2 contributes to the overall I-V characteristics: **(i)** V_S-dominant (pristine MoS_2, $V_S > V_O$) exhibits characteristic abrupt I-V curves from intrinsic V_S filament conduction. **(ii)** V_O-dominant (naturally-oxidized MoS_2, $V_O > V_S$) demonstrates analog *I-V* behavior governed by interfacial V_O migration. **(iii)** Defect-enhanced (plasma-treated oxidized MoS_2, $V_S > V_O$): This process increases the concentration of V_S and other defect types while preserving the intrinsic characteristics of the switching layer, thereby yielding hybrid *I-V* characteristics.

3.1 MoS_2-based Volatile Resistive Switching Devices

The MoS_2-based resistive switching device was fabricated with a typical sandwich structure (**Fig. S1** in the ESM). The bottom electrode (BE) Pt/Ti is deposited onto SiO_2/Si substrate via magnetron sputtering in an Ar atmosphere. The resistive switching layer was subsequently formed via spray coating. The top electrode (TE) was fabricated by depositing Ti. The fabrication process of the device is shown in **Fig. S1**, additional information can be found in the Materials and Experimental Section.The pristine MoS_2 (P-MoS_2) device exhibits typical abrupt *I-V* characteristics and non-volatile behavior, as shown in **Fig. S2** in the ESM, consistent with previous research reports[27, 28]. In contrast, the naturally-oxidized MoS_2 device (O-MoS_2) demonstrated analog bipolar switching behavior (**Fig. 2(a)**). This indicates that the device is governed by interfacial mechanisms rather than localized conductive filament formation. The *I-V* curve exhibits initial LRS and a slight negative differential resistance (NDR) effect from 2.5 V to 6 V, which could be due to a reduction in available electronic states[29]. Furthermore, the I-V characteristics of the device demonstrate excellent long-term stability, retaining a well-defined resistive switching window even after 4 months (**Fig. S3** in the ESM). To investigate the operation mechanisms of the device, the Schottky emission model and Fowler-Nordheim (F-N) tunneling model are utilized to fit the distinct regions of the *I-V* curve (**Fig. S4(a)-(d)** in the ESM). The barrier height of LRS is 480 meV, and HRS is 700 meV, respectively. Compared to the Schottky barrier height of 93 meV for P-MoS_2[27], the O-MoS_2 device demonstrates a significant increase in Schottky barrier height, which effectively impedes the transportation of electrons, accounting for the low current level and higher set/reset voltages. Moreover, the device demonstrated a pronounced tendency to revert from LRS to the HRS during retention testing (**Fig. 2(b)**). At a reading voltage of -0.5 V, the current level of the LRS drops from 2×10^{-7} A to 10^{-11} A, which is almost the same as that of HRS after 600 s. The current decay of the LRS, which could also represent the forgetting rate of the human brain, can be well fitted with the double-exponential decay function (**Fig. S5** in the ESM)[30]. This relaxation phenomenon indicates the volatile feature of the device, and the tendency may be related to the trapping and de-trapping of electrons. The device also exhibited no significant failure characteristics after undergoing over 450 cycles of HRS/LRS switching (**Fig. 2(c)**), while maintaining a switching ratio of more than 10^2.

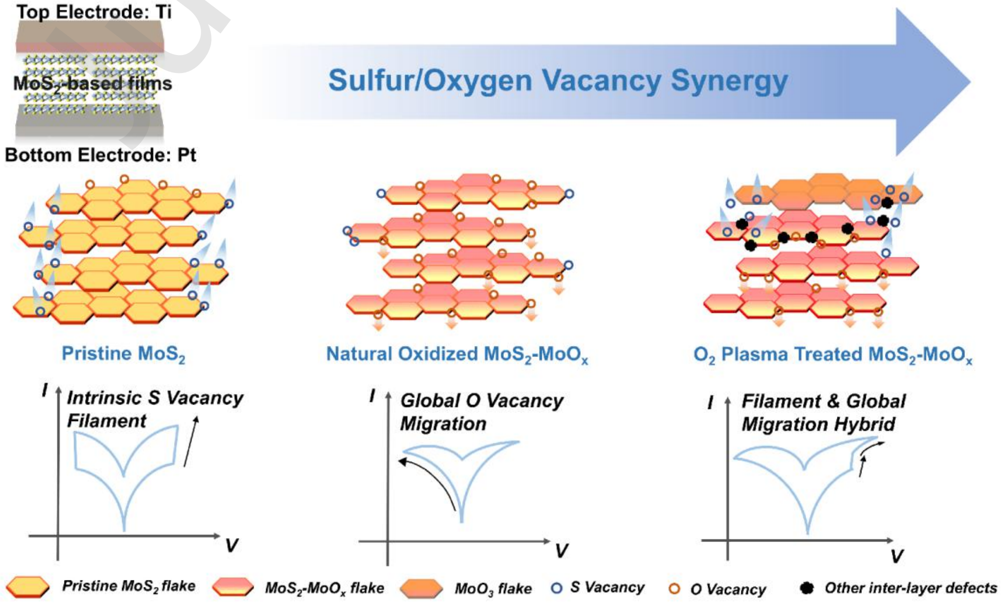

Figure 1 Schematic of the research framework, and sulfur/oxygen vacancies conduction mechanisms within the MoS_2 (MoS_2-MoO_x) switching layer.

Subsequently, the synaptic properties of the O-MoS_2 device were tested. First, we tested the short-term memory (STM) to long-term memory (LTM) behavior by applying three voltage pulse protocols with distinct amplitudes to the O-MoS_2 device. Following sequential voltage stimuli, all curves exhibited characteristic decay behavior. The main decay coefficient (τ_2) extracted by the double-exponential function decay, which increased from 7.60 at -3 V to 12.34 at -5 V, demonstrated the enhancement of the memory characteristics (**Fig. S6(a)** in the ESM). Similarly, we apply different numbers of voltage pulses and different voltage pulse intervals to the O-MoS_2 device to simulate the effects of the numbers and temporal intervals of external stimuli on neural synapses (**Fig. S6(b)-(c)** in the ESM). Both configurations achieved consistent changes in the decay coefficient. Compared to voltage pulse modulations with denser temporal intervals, the pulse modulation characterized by higher amplitude and increased pulse number demonstrates a more pronounced transition of the device from STM to LTM. Next, we investigated the LTP and LTD characteristics of the O-MoS_2 device. We implement two distinct voltage pulse application protocols. The first protocol consisted of applying voltage pulses with identical amplitude and duration to emulate LTP characteristics, subsequently followed by linearly increasing pulse amplitudes from 0.5 V to 4 V to emulate LTD behavior (**Fig. S7(a)** in the ESM). During LTP characterization, three distinct voltage amplitudes (-2.5 V, -3 V, and -3.5 V, pulse width = 25 ms) are applied to the device with a fixed pulse number of 100 for each amplitude set (**Fig. S7(b)** in the ESM). The dynamic conductance range ($G_{\max}/G_{\min}$) exhibits significant enhancement from approximately 35.4 at -2.5 V to 337.6 at -3.5 V. Furthermore, modulation with identical voltage amplitude (-3.5 V, pulse width = 25 ms) but varying pulse counts (50, 100, 150, and 200 pulses) exhibits a well-defined monotonic relationship (**Fig. S7(c)** in the ESM), the conductance ratio $G_{\max}/G_{\min}$ increased from 121.7 at 50 pulses to 560.8 at 250 pulses. Although this programming protocol enables a wide conductance modulation range, its symmetry and nonlinearity remain inadequate.

Accordingly, we implemented a second protocol employing linear voltage ramps from -0.5 V to -4 V (for potentiation) and from 0.5 V to 4 V (for depression). Compared to the first protocol, this scheme enables improved symmetry while maintaining a wide dynamic conductance range (**Fig. S8** in the ESM). Moreover, the device retained functional LTP/LTD characteristics after exposure to over 2×10^4 voltage pulses, signifying exceptional endurance (**Fig. S9** in the ESM). Compared to the first voltage pulse application protocol, the second protocol demonstrates substantial potential for dynamic conductance range modulation. Moreover, the O-MoS_2 device shows no significant degradation after 10^5 voltage pulses, with $G_{\max}/G_{\min}$ maintaining a high value of ~85 (**Fig. 2(d)**), proving the exceptional LTP/LTD robustness of the device. We further increased the pulse counts to 255 for both potentiation and depression, achieving a remarkable G_{max}/G_{min} ratio of 1200 (**Fig. 2(e)**). Comparison of MoS_2-based neuromorphic devices shown in **Fig. 2(f)** reveals that our O-MoS_2 device significantly outperforms prior studies (More details are shown in **Table S1** in the ESM) in LTP/LTD cycling endurance and dynamic conductance range.

We further implemented a four-layer neural network simulation to evaluate the performance of the device on MNIST, Fashion-MNIST, and small-MNIST datasets through simulation (**Fig. S10(a)** in the ESM). The system achieves a high recognition accuracy of 96.05%, 92.21%, and 83.60% for 8×8 small-MNIST, 28×28 MNIST, and Fashion-MNIST databases, respectively (**Fig. S10(b)-(d)** in the ESM). The exceptional dynamic conductance range and relatively low cycle-to-cycle variation during LTP/LTD cycling tests are contributing to the high recognition accuracy[31]. The pattern recognition accuracy can be further increased by improving the linearity in the LTP/LTD performance. Overall, the high robustness and dynamic range of the synaptic behavior, good simulation behavior in pattern recognition, demonstrate the high potential of our O-MoS_2 device for neuromorphic computing applications.

3.2 MoS_2-based Non-volatile Resistive Switching Devices

To further modulate the V_O, V_S, and other types of defects in the switching layer, we subjected the naturally-oxidized MoS_2 films to oxygen plasma treatment. We employed O_2 plasma treatment (200 W power) on MoS_2-MoO_x hybrid films for 10, 20, and 30 minutes[32-34], followed by device fabrication the same as the untreated MoS_2-MoO_x device (**Fig. 3(a)**). Initial *I-V* characterization (**Fig. 3(b)-(d)**) reveals that the O_2 plasma-treated device exhibits different resistive switching characteristics compared to their naturally-oxidized and pristine counterparts: **(i)** Plasma-treated devices (particularly 10-min and 20-min) exhibit hybrid filament-interface switching characteristics, in contrast to P-MoS_2 devices exhibiting filament characteristic and O-MoS_2 devices demonstrating interface-dominant behavior. **(ii)** All O_2 plasma-treated devices exhibited an initial HRS compared to that in naturally-oxidized MoS_2. The devices subjected to 10-min (10-MoS_2) and 20-min (20-MoS_2) O_2 plasma treatments retain relatively large switching windows (~10^2), while the switching window of the device after 30 min O_2 plasma treatment (30-MoS_2) is significantly narrowed (<10). This could be due to the fact that a prolonged oxygen plasma bombardment introduces a higher density of defect states and sulfur vacancies into the MoS_2-MoO_x thin film, compromising the ON/OFF ratio. We evaluated the long-term stability of the *I-V* characteristics of the plasma-treated devices, and all devices maintained relatively stable *I-V* characteristics for over three months (**Fig. S11(a)-(c)** in the ESM). Furthermore, retention tests (**Fig. S12(a)-(c)** in the ESM) revealed stable ON/OFF ratios for over 10^3 seconds. We further investigated their multilevel resistance state capabilities. For the 10-MoS_2, 13 distinct current states were achieved through stepwise pulse voltage modulation (set from 0.1 V to 4 V) within a current compliance range of 5×10^{-5} A to 1×10^{-3} A, with each state demonstrating a retention time of >100 s (**Fig. 3(e)**). The standard deviation (Δ) and mean value (μ) for each current state were calculated. The coefficient of variation (Δ/μ) values for all 13 distinct current states are substantially lower than the relative change between adjacent states (**Fig. S13(a)** in the ESM), indicating excellent stability and low fluctuation characteristics. Correspondingly, the number of multilevel current states for the 20-min(voltage set from -0.5 V to -4 V) and 30-min (voltage set from -0.1 V to -3 V) treated devices reaches 11 and 9, respectively (**Fig. 3(f)-(g)**). Each state calculation is similar to the 10-MoS_2(**Fig. S13(b)-(c)** in the ESM), and all exhibited characteristics where Δ/μ values were much underwent statistical lower than the

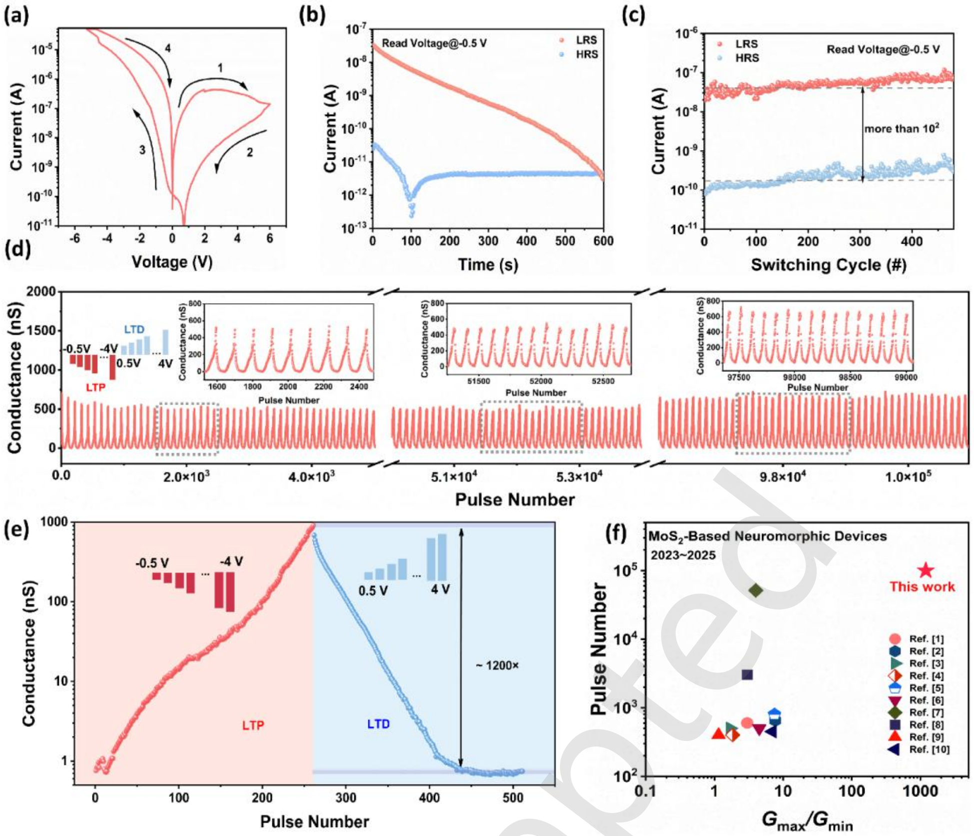

Figure 2 Synaptic characteristic emulation of the naturally-oxidized MoS_2 (O-MoS_2) volatile device. **(a)** Representative *I-V* curve. **(b)** Retention test for both LRS and HRS. **(c)** Endurance test under DC voltage sweep. **(d)** LTP/LTD cycling test exceeding 10^5 voltage pulses. **(e)** LTP/LTD modulation via symmetric linear voltage ramping (-0.5 to -4 V and 0.5 to 4 V), 255 voltage pulses for LTP and 255 pulses for LTD. **(f)** Comparison of dynamic conductance ranges and pulse number with representative MoS_2-based neuromorphic studies.

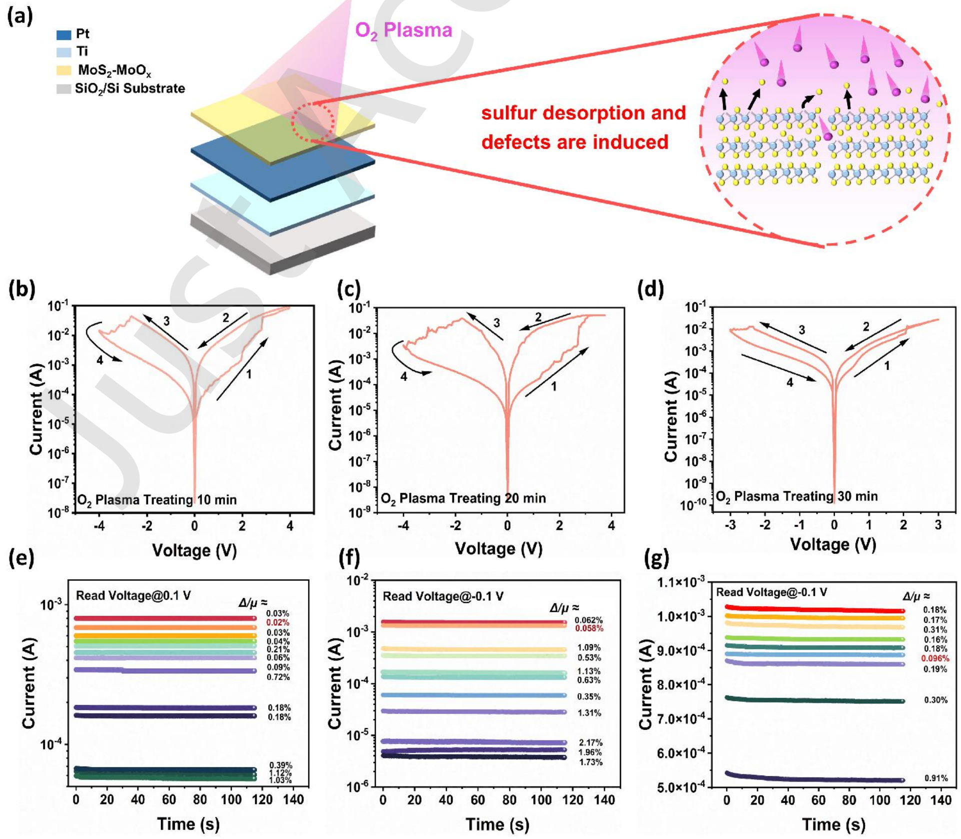

Figure 3 Electrical properties and multilevel behavior of O_2 plasma-treated MoS_2-MoO_x device. **(a)** Schematic illustration of oxygen plasma processing for the MoS_2-MoO_x hybrid films. Ti electrodes are fabricated after the plasma treatment process. **(b)-(d)** Typical *I-V* curves of devices treated with 10, 20, and 30 min O_2 plasma. **(e)-(g)** Multilevel current states of 10-min, 20-min, and 30-min O_2 plasma-treated device.

variation values between adjacent states, proving the usability of all multilevel states. The minimum Δ/μ values reach as low as

10^{-4}, indicating exceptional stability across multiple conductance states and a strong potential for circuit-level RRAM applications. Remarkably, compared to approaches requiring multi-component switching layers or complex fabrication processes reported elsewhere, our single-step plasma modulation of MoS_2 and its native oxide achieves comparable multi-state stability[35, 36].

3.3 Materials Characterization

Field-emission transmission electron microscopy (FETEM) characterization was performed on P-MoS_2, O-MoS_2, and O_2 plasma-treated MoS_2-MoO_x (Plasma-MoS_2) films to analyze lattice arrangement and the spatial distribution of sulfur and oxygen elements. **Fig. 4(a)** shows the lattice structure of P-MoS_2, with the corresponding fast Fourier transform (FFT) pattern provided in the inset. Analysis reveals two distinct lattice orientations in P-MoS_2, with interplanar spacings of 0.27 nm and 0.16 nm, corresponding to the (002) and (100) planes, respectively[37]. Despite the absence of oxidation treatments, P-MoS_2 exhibits well-ordered lattice fringes while still retaining intrinsic sulfur vacancies. **Fig. 4(b)** and **Fig. 4(c)** present the elemental mapping of sulfur and oxygen in P-MoS_2. While no MoO_x phase is detected in the FFT pattern, elemental mapping of P-MoS_2 reveals an oxygen content of approximately 10%. This is likely attributable to the adsorption of ambient O_2 and H_2O molecules on the MoS_2 surface. For the O-MoS_2, the FFT pattern indicates a composite of two distinct materials: one set of diffraction spots corresponds to the MoS_2 lattice planes consistent with P-MoS_2, while an additional set is indexed to the (111) plane of MoO_x (**Fig. 4(d)**). The formation of an oxide phase, resulting in a mixed MoS_2-MoO_x state, is further evidenced by sulfur elemental mapping (**Fig. 4(e)**) and a substantially increased oxygen content of 16% revealed in the O mapping (**Fig. 4(f)**). Similarly, O_2 plasma-treated MoS_2-MoO_x (Plasma-MoS_2) shows coexistence of the (002) plane of MoS_2 and the (111) plane of MoO_x (**Fig. 4(g)**). Notably, O_2 plasma bombardment introduces structurally damaged regions with significantly elevated concentrations of defects. Quantitative elemental analysis of **Fig. 4(h)** and **Fig. 4(i)** reveals that, compared to O-MoS_2, the oxygen content in Plasma-MoS_2 increased to 23%, while the sulfur content decreased from approximately 52% to about 46%, indicating intensified oxidation and concomitant sulfur desorption.

Molybdenum elemental mapping is provided in **Fig. S14(a)-(c)** in the ESM. The content decreased from approximately 33% in both P-MoS_2 and O-MoS_2 to about 31% in Plasma-MoS_2, which likely reflects the partial desorption of Mo atoms and the concomitant formation of Mo vacancies. Overall, the TEM results confirm that both natural oxidation and oxygen plasma treatment influence the lattice arrangement, defect generation, and formation of oxide products in MoS_2. These structural and chemical modifications are likely responsible for the distinct resistive switching behaviors observed in differently processed MoS_2 samples.

Furthermore, the chemical information of the MoS_2/MoS_2-MoO_x nanosheets was examined by Raman spectra first (**Fig. S15(a)** in the ESM). Under the incidence of a 532 nm wavelength laser, the typical MoS_2 peaks are located at 379 cm^{-1} and 404 cm^{-1}, respectively, corresponding to MoS_2 E_{2g} and A_{1g} vibration modes[38]. The A_{1g}-E_{2g} vibrational separation $\Delta \approx 25$ cm^{-1}, demonstrating the film is assembled by multi-layer MoS_2 nanosheets[24]. On the other hand, the longitudinal acoustic (LA) phonon mode of MoS_2 near 226~227 cm^{-1} serves as an indicator of inter-layer defects (including sulfur vacancies, antisite defects, and Mo-related defects)[39]. Compared to typical Raman spectra of MoS_2, prolonged oxygen plasma treatment induced a red shift in the E_{2g} peak and a slight blue shift in the A_{1g} peak. The E_{2g} mode shift indicates weakened inter-layer van der Waals interactions, suggesting that structural modifications from multi-layer stacking or inter-layer Coulomb coupling predominantly govern the atomic vibrational changes[40]. Conversely, the A_{1g} mode alteration predominantly could be attributed to increased sulfur vacancy formation within the MoS_2 lattice[41]. In addition, we also observed small peaks appear at about 302 cm^{-1} and 987 cm^{-1}, corresponding to the MoO_3 B_{1g} bending mode and terminal oxygen asymmetric stretching of Mo=O (Ag mode), respectively, confirming the oxidation of the MoS_2[42]. The monotonic increase in A_g/B_{1g} intensity ratio (**Fig. S16** in the ESM) is likely due to the formation of more completely oxidized MoO_3 on the surface and elevated defect concentrations in MoO_3 domains, consistent with peak effects observed in MoS_2 phase analysis. UV-Vis spectroscopy (**Fig. S15(b)** in the ESM) of the switching films reveals that the naturally-oxidized MoS_2-MoO_x has a band gap of ~3.28 eV, corresponding to bulk MoO_3. After O_2 plasma treatment, the band gap increased slightly to 3.32 eV (10 min) and further to ~3.41 eV (20-30 min), attributed to the formation of nanoscale MoO_3 domains and quantum confinement effects[43-45]. XRD analysis (**Fig. S15(c)** in the ESM) confirms the composite nature and orientation. Pristine MoS_2 shows a dominant (002) peak at 14.50°, indicating highly oriented exfoliation. In contrast, plasma-treated films exhibit distinct MoO_3 peaks (e.g., 40.10°, 50.10°, 55.14°, 68.34°) indexed to (150), (112), and (0100) planes. Together, these results confirm that oxygen plasma promotes surface MoO_3 formation, resulting in a composite film of multilayer MoS_2 and MoO_x[46].

XPS characterization was further performed on pristine-MoS_2 and MoS_2-MoOx films to analyze the changes in chemical composition. **Fig. 4(j)-(m)** presents the sulfur XPS spectra of different types of MoS_2-based films. Both P-MoS_2 and O-MoS_2 exhibit S $2p_{1/2}$ and $2p_{3/2}$ binding energies near 162.45 eV and 163.65 eV, slightly higher than the typical sulfur binding energy. The binding energy peak of S $2p_{3/2}$ for 10-MoS_2 and 20-MoS_2 increases, implying the downshift of the Fermi level[47]. Moreover, an additional binding energy peak at ~163 eV was deconvoluted in the S 2p XPS spectra of P-MoS_2, O-MoS_2, and 10-MoS_2, attributed to sulfur vacancies or defects resulting from desorbed sulfur atoms[8, 48]. For the 20-MoS_2, the spectral signature evolves from a single peak to doublet splitting, suggesting the transformation of dispersed V_S into aggregated V_S clusters under prolonged oxygen plasma bombardment. This structural reorganization induces significant alterations in the chemical environment of vacancy sites. The Mo 3d XPS spectra of P-MoS_2, O-MoS_2, 10-MoS_2, and 20-MoS_2 are presented in **Fig. S17(a)-(d)** in the ESM. From P-MoS_2 to 20-MoS_2, intermediate species (e.g., MoO_x and defected-MoS_2) exhibit a trend of initial increase followed by a decrease during progressive oxidation. The O 1s XPS spectra are shown in **Fig. S18(a)-(d)** in the ESM. Similar to the trend exhibited by the XPS spectrum of Mo, the V_O concentration also shows a trend of first increasing and then decreasing. In summary, the XPS spectra of Mo, O, and S successfully confirm that our sulfur and oxygen vacancy modulation strategy is effective. For the 30-MoS_2, the sulfur XPS spectrum exhibits a marked difference **(Fig. S19** in the ESM): The oxidation of S^{2-} ions to higher-valence SO_4^{2-} species, coupled with partial sulfur volatilization as SO_2 and the rapid attenuation of S $2p_{1/2}$ and $2p_{3/2}$ peak intensities, suggests a significant increase in sulfur vacancy concentration within 30-MoS_2 compared to its 10-min and 20-min counterparts. Collectively, the XPS elemental analysis corroborates the results from TEM, leading to a congruent conclusion.

Based on the deconvolved XPS data of all samples (excluding 30-MoS_2), we quantified the relative proportions of V_S and V_O on an elemental basis (**Fig. 4(n)**). Since prolonged oxygen plasma treatment reduces the overall sulfur content while increasing oxygen content, our normalized statistics—expressed as the $V_O(V_S)/(O+S)$ ratio relative to the total sulfur and oxygen content—better reflect relative changes in vacancy dominance. For P-MoS_2, V_S predominates over V_O, indicating that V_S governs the resistive switching behavior. In contrast, O-MoS_2 exhibits an inverse trend to P-MoS_2, characterized by reduced V_S concentration and increased V_O density. This phenomenon originates from ambient oxygen incorporation occupying VS sites in MoS_2, forming oxygen-deficient $MoS_{2-x}O_x$ (MoO_x) surface layers. Following O_2 plasma treatment, both 10-MoS_2 and 20-MoS_2 show a marked increase in V_S proportion, which consistently exceeds that of V_O. This confirms the effective introduction of V_S by plasma treatment, leading to renewed dominance of V_S in governing the carrier transport properties of 10-MoS_2 and 20-MoS_2 devices. Additionally, we calculated the $(V_S+V_O)/(S+O)$ atomic ratio across all samples. Following natural oxidation and oxygen plasma treatment, this ratio increased from 19.57% in P-MoS_2 to 24.86% in 20-MoS_2, indicating a moderate increase in total vacancy concentration during our processing. Moreover, we calculated the $I(LA)/I(A_{1g})$ intensity ratio (**Fig. 4(n)**) based on the Raman results in **Fig. S13(a)** in the ESM. This ratio progressively increased from 10% for P-MoS_2 to 40% for 20-MoS_2, demonstrating the generation of inter-layer defects induced by both natural oxidation and plasma treatment. In P-MoS_2, sulfur vacancies constitute the primary inter-layer defect type. However, lattice damage and distortion caused by natural oxidation and oxygen plasma treatment possibly increase the population of antisite defects and Mo-related defects. On the other hand, although our experimental results exhibit a trend that aligns with the theoretical framework, the threshold concentration of vacancies or defects that induces the transition of device characteristics still necessitates a more meticulous investigation.

3.4 Switching Mechanism Analysis

Based on the presented electrical and material characteristics of the MoS_2-based devices, we found that V_O, V_S, and other in-plane defects are key mediators enabling the device transition from a filamentary switching mode to an interface-dominated switching mode, and subsequently to a hybrid switching regime. Informed by this, we conducted mechanism analyses of devices under different processing conditions. The schematic operation mechanism for P-MoS_2 is depicted in **Fig. 5(a)**. Consistent with previous reports, P-MoS_2 exhibits typical conductive-filament switching characteristics, originating from V_S enrichment within the MoS_2 layer, where vacancies migrate via edge sites of the nanosheets to form inherent conductive pathways. Both Schottky emission and Poole-Frenkel tunneling models provide excellent fits to the positive voltage sweep region of the P-MoS_2 *I-V* curves (**Fig. S20(a)-(b)** in the ESM), indicating that current in the HRS and LRS is dominated by thermionic emission and barrier-lowering-induced tunneling, respectively.

As natural oxidation proceeds, the MoS_2 nanosheets transform into an MoS_2-MoO_x hybrid. V_O and some V_S within the MoS_2-MoO_x switching layer exhibit uniform distribution across the hetero interface[27]. Unlike the P-MoS_2 device, the O-MoS_2 device exhibits an initial LRS (**Fig. 5(b)**). Upon applying a positive bias to the TE, V_O and partial V_S that act as n-type dopants migrate collectively towards the BE. This causes the Schottky barrier to decrease gradually, and the device exhibits an LRS. The reduced interfacial barrier enhances electron injection from the switching layer into the metal electrode, causing a downshift of the Fermi level within the switching layer. This reduces the number of available intermediate states, leading to current saturation despite the device remaining in LRS. Upon further increasing the positive bias, a large number of V_O and V_S accumulate near the BE, which introduces a large number of local density of states, and these defect states pin the Fermi level[49]. On the other hand, the accumulation of a large number of vacancies attracts electrons, forming a local electric field[25], which conversely leads to an increase in the barrier height, resulting in the device switching from LRS to HRS. When a negative voltage is applied to the TE, vacancies accumulated at the BE gradually migrate toward the TE. The Fermi level pinning effect and electronic Coulomb screening effect weaken, leading to a decrease in the Schottky barrier, and the device switches from HRS to LRS again. Correspondingly, the transition of the fitting model (including Schottky emission and F-N tunneling) further supports this interpretation.

To back up the proposed mechanism for the naturally-oxidized MoS_2 devices, we further processed the pristine MoS_2 film under oxygen annealing conditions and checked the corresponding *I-V* sweeping behavior (**Fig. S21(a)-(c)** in the ESM). We found a similar analog bipolar behavior where initial LRS is confirmed. Furthermore, fitting of the *I-V* characteristics for annealed MoS_2 revealed excellent agreement with Schottky emission models (**Fig. S22(a)-(d)** in the ESM), consistent with fitting results for O-MoS_2 devices. Notably, compared to O-MoS_2 devices, devices based on annealed MoS_2 film exhibited substantially lower current levels (ILRS ≈ 10^{-7} A) and significantly increased SET/RESET voltages

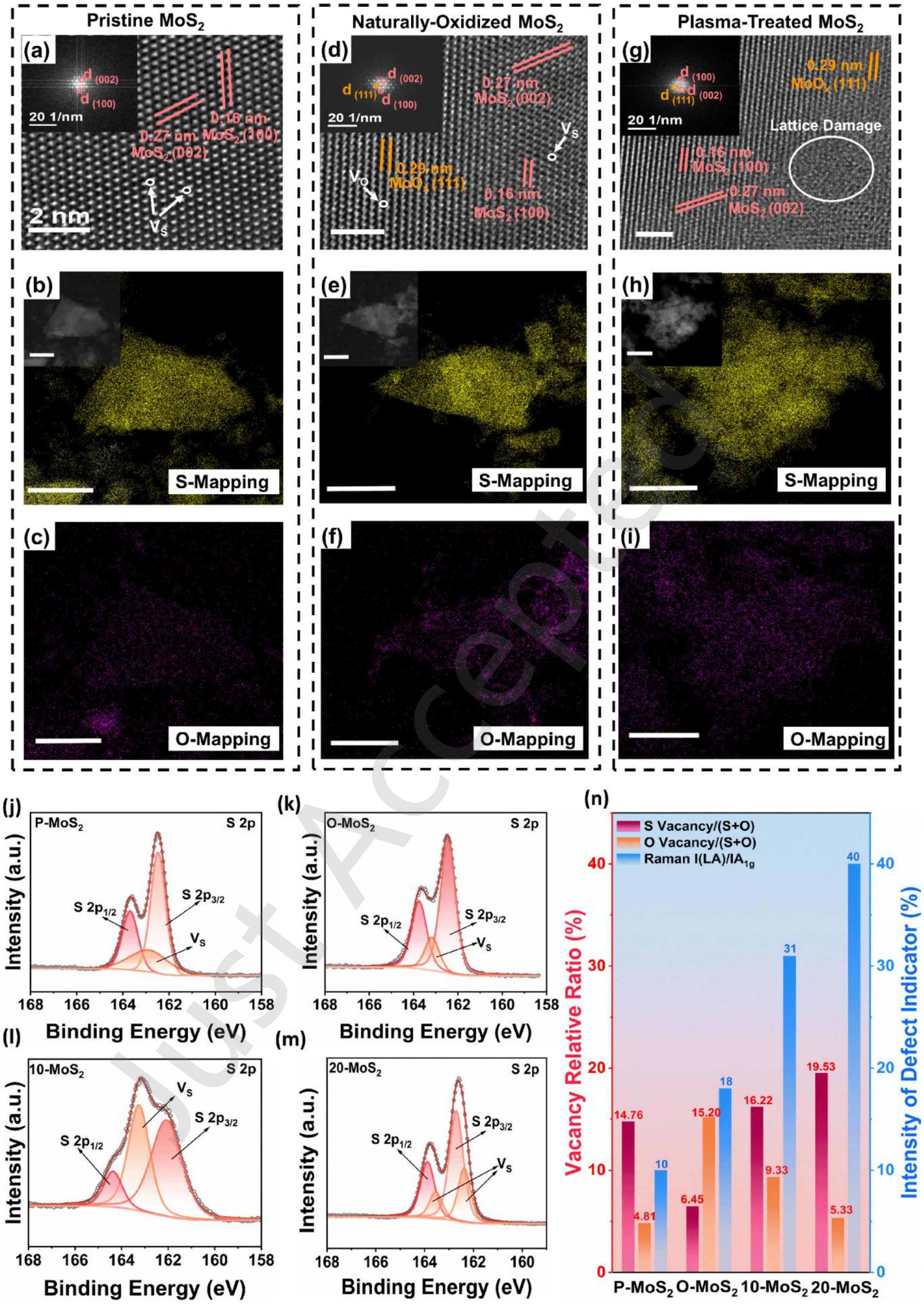

Figure 4 The material characterization of the pristine MoS_2 and MoS_2-MoO_x films. **(a)** Lattice and FFT images of pristine-MoS_2 (P-MoS_2). **(b)** Sulfur and **(c)** oxygen elemental mapping of P-MoS_2, the scale bar is 200 nm. **(d)** Lattice and FFT images of naturally-oxidized MoS_2(O-MoS_2). **(e)** Sulfur and **(f)** oxygen elemental mapping of O-MoS_2, the scale bar is 250 nm. **(g)** Lattice and FFT images of O_2 plasma-treated MoS_2-MoO_x (Plasma-MoS_2). **(h)** Sulfur and **(i)** oxygen elemental mapping of Plasma-MoS_2, the scale bar is 200 nm. Sulfur XPS spectra for **(j)** P-MoS_2, **(k)** O-MoS_2, **(l)** 10-min (10-MoS_2), and **(m)** 20-min (20-MoS_2) O_2 plasma-treated MoS_2-MoO_x. **(n)** Statistical results of V_S and V_O proportion derived from XPS and I(LA)/I(A1g) ratio in Raman spectra for different films. The ratio $V_S(V_O)/(S+O)$ quantifies the proportion of specific vacancy types relative to the total sulfur and oxygen content, enabling identification of the dominant vacancy type governing device mechanisms. Meanwhile, the intensity ratio I(LA)/I(A_{1g}) serves as an indicator of in-plane defect concentration within the switching layer.

(>15 V). This behavior originates from the high-temperature annealing process, leading to a more insulating layer on the MoS_2 surface. Critically, thermal annealing promotes more complete surface oxidation than natural oxidation, yielding fewer sub-stoichiometric oxide products. The energy band diagram of annealed MoS_2 is presented in **Fig. S23** in the ESM. Similar to O-MoS_2, the mild oxidation strategy facilitates oxygen incorporation at partial sulfur vacancy sites, which is different from the oxygen plasma process. The gradient-like distribution of V_O within the switching layer dominates the resistive switching in the device. Moreover, the annealed-MoS_2 device exhibits volatile behavior analogous to that of O-MoS_2 (**Fig. S24(a)-(b)** in the ESM). Therefore, MoS_2 devices subjected to mild oxidation (including both natural and annealing oxidation) undergo a switching mechanism transition from filament (non-volatile) to interface (volatile), which is governed by the global migration of V_O.

Previous discussion concludes oxygen plasma treatment generates more MoO_3, primarily due to the occupation of oxygen atoms into vacancy sites. Meanwhile, bombardment by high-energy oxygen plasma generates additional defects, including V_S, molybdenum vacancies, and substitutional defects. Consequently, the switching layer could be divided into two distinct regions: the region adjacent to the TE consists of MoS_y-MoO_3 with V_S being dominant, while the region near the BE retains the MoS_2-MoO_x configuration dominated by V_O. The schematic of the operation mechanism for plasma-treated MoS_2 is shown in **Fig. 5(c)**. In the initial state, the device resides in the HRS. Upon application of a positive voltage to the TE, conductive filaments form within the MoS_y-MoO_3 layer and extend into the MoS_2-MoO_x layer, accounting for the initial abrupt switching behavior observed in the *I-V* characteristics. As the voltage further increases, V_O previously adsorbed at metal vacancy sites gradually detach and migrate toward the BE[50], imparting partial interface-dominant characteristics to the *I-V* curve. The synergistic effect of these processes drives the transition from HRS to the LRS, and the *I-V* curve exhibits hybrid conductive-filament/interface-mediated transport behavior. When the voltage switches from positive to negative, V_S in the MoS_y-MoO_3 layer migrates toward the TE, leading to progressive dissolution of the conductive filament. Simultaneously, V_O in the MoS_2-MoO_x layer migrates upward from the BE and undergoes re-adsorption, collectively driving the device transition from LRS to HRS. Moreover, fitting results for the LRS and HRS of the 20-MoS_2 device are shown in **Fig. S25(a)-(b)** in the ESM. These results demonstrate that the conduction mechanism in the HRS follows the Schottky emission model. Upon switching to the LRS, the operating mechanism transitions to the trap-assisted tunneling model, consistent with our proposed mechanism. Similar mechanisms have been reported in related studies, and the devices exhibited electrical characteristics analogous to those observed in our work, providing support for the proposed framework model. Further microscopic characterization is required to achieve a comprehensive understanding of this hybrid mechanism[51-53].

Based on our analysis and fitting results, we conclude that when intrinsic V_S concentration exceeds V_O density in MoS_2-based devices, Schottky emission and Poole-Frenkel tunneling (electron trapping at edge sulfur vacancies forming bound states) is the dominant model. Conductive filament formation via V_S migration along MoS_2 nanosheet edges governs the resistive switching mechanism, demonstrating abrupt nonvolatile *I-V* characteristics. When oxidized characteristics emerge in the switching layer with $V_O > V_S$, global V_O migration becomes the dominant mechanism, transitioning device *I-V* characteristics from abrupt non-volatile switching to analog volatile switching. Further increasing the concentration of other defect types and V_S by plasma treatment induces non-volatile hybrid switching behavior. Synergistic effects between shallow defect levels and vacancies are consistent with trap-assisted tunneling. The conductive filament formation (Induced by V_S) and V_O migration are contributing together to the mechanism transition. Moreover, synergistic effects between shallow defect levels by additional defects and vacancies facilitate the transportation of electrons. Moreover, we noticed that resistive switching devices based on pristine MoS_2 nanosheets exhibit *I-V* curves with typical abrupt switching characteristics[27, 54-56], whereas this feature is significantly weakened in partially oxidized MoS_2 ($MoS_{2-x}O_x$), which even displays gradual *I-V* curves[19, 24, 57]. The physical mechanisms of these two types of devices are often discussed based on the transport of different types of vacancies, which further supports our hypothesis for the mechanism of MoS_2-based devices.

3.5 Neuromorphic Circuits Including Volatile and Non-volatile Devices

By controlling the relative concentrations of V_S, V_O, and other in-plane defects, we successfully achieved high-performance volatile and non-volatile MoS_2-based devices. Leveraging this capability, we explored scenarios for homogeneous integration of different device behaviors from MoS_2 devices in hardware neural networks. We designed a spike-response model (SRM)-based neuromorphic circuit incorporating both volatile (O-MoS_2) and non-volatile (10-MoS_2) devices. The SRM circuit integrates an adaptive threshold modulation module, which is based on the leaky integrate-and-fire (LIF) framework. The module enables emulation of advanced neuronal functionalities—including refractory periods (temporary unresponsiveness post-activation) and lateral inhibition (suppressive interactions between adjacent neurons)—beyond conventional LIF capabilities[58]. Previously reported volatile memristors for LIF circuits pose challenges in external component control and introduce operational uncertainties[59]. The SRM circuit integrates an adaptive threshold modulation module, which is based on the leaky integrate-and-fire (LIF) framework. The module enables emulation of advanced neuronal functionalities—including refractory periods (temporary unresponsiveness post-activation) and lateral inhibition (suppressive interactions between adjacent neurons)—beyond conventional LIF capabilities[58]. Previously reported volatile memristors for LIF circuits pose challenges in

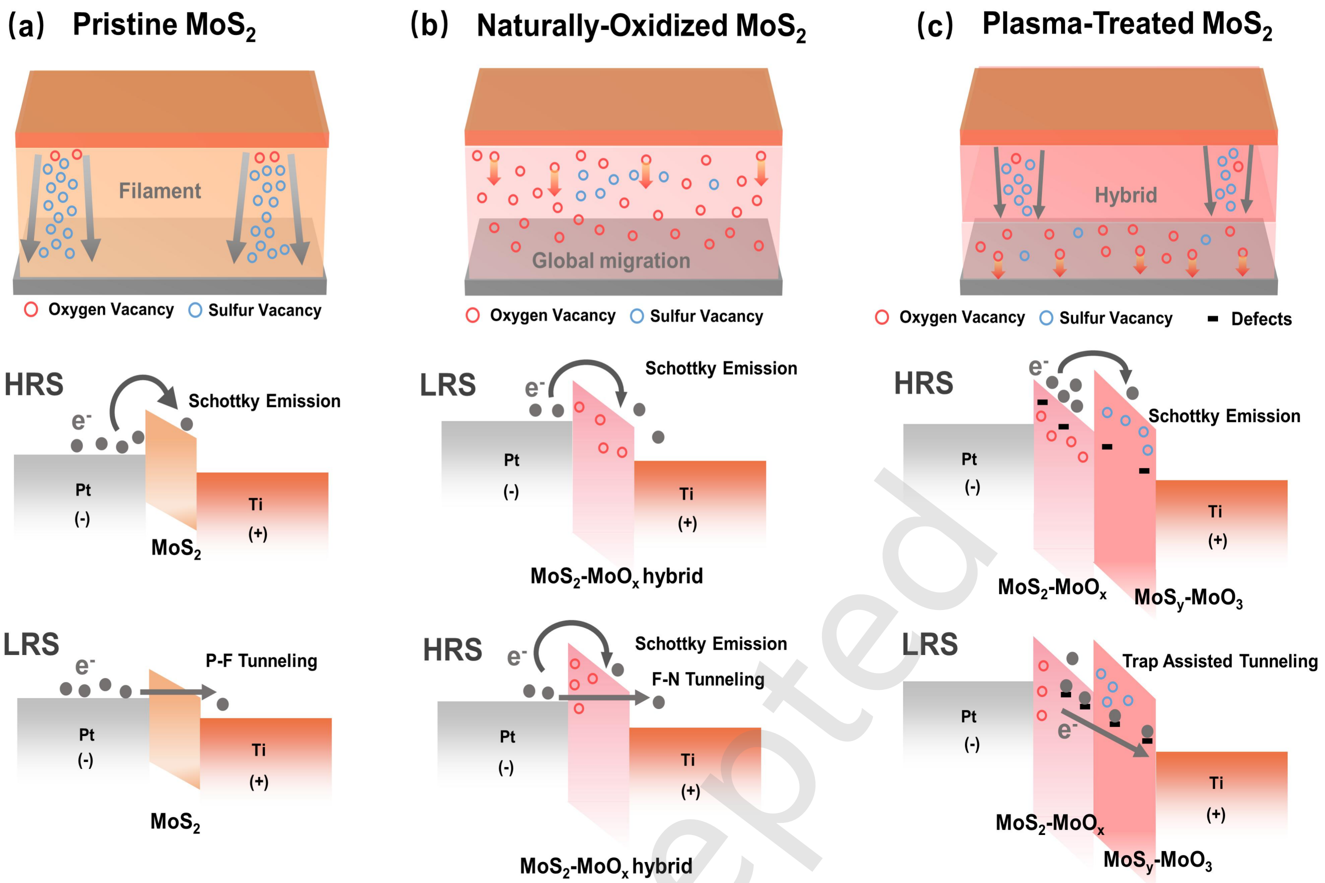

Figure 5 Schematic diagrams of the resistance switching mechanism of the pristine MoS_2 device, naturally-oxidized MoS_2 device, and O_2 plasma-treated MoS_2-MoO_x device. **(a)** Schematic mechanism illustrations and HRS/LRS energy band diagrams for the P-MoS_2 device. The dominant transport mechanism involves sulfur vacancy migration along intrinsic defect sites within MoS_2 nanosheets. The Schottky emission model and the P-F model could emulate the electron transport process. **(b)** Schematic illustrations of V_O migration and HRS/LRS energy band diagrams for the O-MoS_2 device. The primary operating mechanism relies on the global migration of V_O. As vacancy aggregation enhances the Coulombic screening effect, the Schottky barrier height between the MoS_2-MoO_x/metal interface increases, leading to a transition of LRS to HRS. **(c)** Schematic mechanism illustrations of HRS/LRS energy band diagrams for the plasma-treated MoS_2 device. The dominant operation mechanism involves conductive pathways of V_S vacancy (near TE) and V_O global migration (near BE).

external component control and introduce operational uncertainties[59]. whereas our approach utilizes non-volatile memristors with specific set/reset voltages in an SRM-based architecture that preserves neuronal functionality, enhances control precision and reliability, and simplifies connectivity compared to models like the spike-frequency adaptive model[60]. Furthermore, SRM-enabled SNNs trained with the unsupervised SRDP rule exhibit superior hardware compatibility and are promising for applications requiring enhanced pattern recognition and feature extraction[61]. The full circuit architecture is shown in **Fig. 6(a)**. The SRM neuronal circuit comprises two modules: the LIF module and the threshold adaptation module. The LIF module integrates a non-volatile memristive device (mem1, using 10-MoS_2), a comparator (LM393), and a pulse generator (NE555). Mem1 forms a voltage divider with resistor Rm to emulate the neuronal membrane potential (Vmem1). The inverting input of the LM393 shares the same potential as Vmem1. When the potential at the inverting input exceeds that at the non-inverting input (i.e., the threshold voltage V_{th}), the output signal from the LM393 triggers the NE555, generating a fixed-duration positive output pulse. The threshold adaptation module consists of a volatile memristive device (mem2, using O-MoS_2) and a multiplexer (MUX). The MUX receives input from the LIF output (V_{out}) and other signal sources, emulating neuronal refractory periods and lateral inhibition functionalities while generating an output voltage signal. Ultimately, changes in the resistance of mem2 alter the voltage division with resistor R_{th}. This dynamically adjusts the V_{th}, thereby controlling the output pulse generation of the LM393.

Owing to more stable current-voltage characteristics, non-volatile devices enable two distinct firing modes: charge-accumulation-triggered (As the number or amplitude of electrical pulses increase, the migration of vacancies or electrons within the switching layer is enhanced, leading to resistive state switching) firing in the HRS (**Fig. S26(a)** in the ESM) and immediate spiking (The device switches to a stable LRS, and each input spike enables fixed voltage division and firing) in the LRS (**Fig. S26(b)** in the ESM). In contrast, volatile devices, constrained by relaxation dynamics and stochastic behavior, exhibit significantly less deterministic neuronal firing probability compared to non-volatile counterparts, and could only achieve charge-accumulation-triggered mode. We first implement the charge-accumulation-triggered firing mechanism to construct the SRM neuronal circuit. Initially, input voltage pulses (V_{in} in **Fig. 6(b)**) are applied to the non-volatile device mem1. As charge accumulates gradually, mem1 switches from HRS to LRS, and the node voltage Vmem1 exceeds the preset threshold voltage. Consequently, an output action potential spike V_{out} is triggered. In the absence of lateral inhibition from other neurons (V_{ext} represented in **Fig. 6(b)**), this output spike subsequently modulates the resistive state of mem2 via a multiplexer, switching mem2 from HRS to LRS. The resulting voltage division at R_{th} increases V_{th} beyond V_{mem1}, thereby inhibiting V_{out} and spike generation. Due to the volatile characteristics of mem2, its resistance recovers to HRS, reducing V_{th}. Once V_{th} falls below V_{mem1} again, action potential generation will resume at V_{out}. This adaptive regulation process exhibits strong resemblance to the refractory period dynamics of biological neurons, which can be used for the adaptive regulation of the output layer in neural networks[54]. Regarding lateral inhibition from other neurons (**Fig. 6(c)**), when spikes from other neural units are applied to the multiplexer (pink traces in **Fig. 6(c)**), the lateral inhibitory voltage pulse pathway is activated. This pulse switches mem2 from HRS to LRS, elevating V_{th} above V_{mem1} and consequently suppressing action potential generation at V_{out}. This process demonstrates threshold modulation of the SRM neuron by another neuron. Evidently, compared to the single LIF circuit, our SRM circuit successfully emulates neuronal refractory periods and lateral inhibition effects, achieving more biologically plausible neuronal functionalities. Furthermore, comparable outcomes were achieved in emulating fixed pulse amplitudes in response to sensitive stimuli (**Fig. S27(a)-(b)** in the ESM). The SRM neuronal characteristics exhibit strong alignment with the requirements of the unsupervised SRDP learning rule[58]. This synergy enables the hardware implementation of SNNs with efficient learning attributes. Moreover, compared with circuits composed of volatile devices, the LIF module constructed using non-volatile memristors in our work demonstrates enhanced firing stability and increased firing activity.

Moreover, refractory periods and lateral inhibition effects realized by the SRM model in our homogeneous design protocol promote a "winner-takes-all" effect in SNNs trained under the SRDP rule, thereby enhancing learning efficiency and recognition accuracy compared to that without SRM[61]. Furthermore, the utilization of non-volatile devices in the SRM circuit enables immediate generation of output spikes, while significantly enhancing the circuit stability and controllability compared to that fabricated solely with volatile devices. These characteristics are highly suitable for scenarios requiring feature extraction and enhanced recognition, such as speech recognition and voiceprint extraction. To this end, we propose a software-hardware collaborative SNN based on SRM for such scenarios (**Fig. 6(d)**). At the hardware level, the memristor array performs computation and storage on encoded input spikes and outputs signals to the SRM circuit. The SRM circuit functions corresponding to the output layer of the SNN with adaptive threshold modulation and lateral inhibition capabilities, thereby enabling feature enhancement and feature recognition-extraction. Furthermore, the different defect engineering approaches demonstrated in this study are fully compatible with the proposed concept of homogeneous integration. For instance, the integration of devices with different electrical characteristics on the same chip can be achieved using the same material through techniques such as selective native oxidation or local oxygen plasma treatment[62].

4 Conclusions

In conclusion, via sulfur/ oxygen vacancies synergistic defect engineering protocol, we successfully realized a switching mechanism transition in MoS_2-based resistive switching devices, from non-volatile (filament) to volatile (interface), finally non-volatile (hybrid). The volatile device exhibited a high robustness over 105 voltage pulses in the LTP/LTD cycling test and a maximum dynamic conductance range of 1200, highlighting significant potential for neural network computing. Meanwhile, the nonvolatile device exhibited up to 13 distinct stable resistance states, with an ultralow Δ/μ ratio as low as 10^{-4}, promising for multilevel resistance storage. The switching mechanism transition was attributed to the dominant switching species modulation from sulfur vacancies to oxygen vacancies, which further changes the underlying charge transport characteristics. Furthermore, by integrating these volatile and non-volatile devices, we successfully constructed a homogeneous SRM circuit capable of different firing modes and adaptive threshold modulation such as refractory periods and lateral inhibition in neuron transmission, which demonstrates promising potential for high-accuracy speech processing scenarios within a hardware-software co-designed SNN architecture. In short, the proposed synergistic mechanism involving sulfur and oxygen vacancies offers a concise understanding and a promising strategy for modulating resistive switching. This approach is applicable not only to MoS_2 -based devices but also to other oxidation-prone TMDs (e.g., sulfides, selenides, tellurides) and related nanomaterials, facilitating their homogeneous integration in neuromorphic computing.

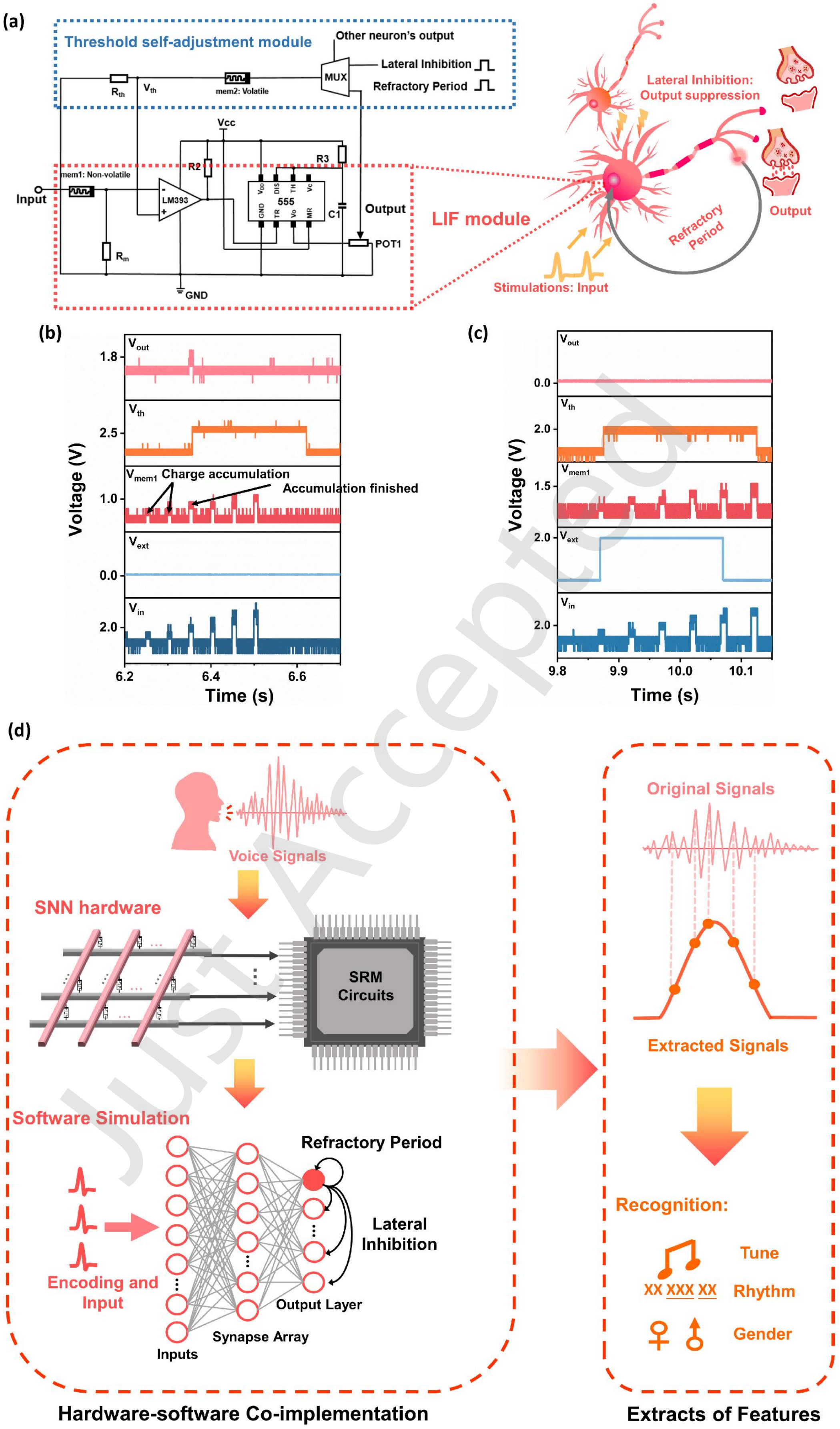

Figure 6 SRM neuron circuit and application composed of the non-volatile 10-MoS$_2$ device and the volatile O-MoS$_2$ device. **(a)** Schematic of the SRM circuit. The red box denotes the LIF module, and the blue box denotes the threshold adjustment module. **(b)** Voltage pulse waveforms for the function of refractory period (neurons no longer generate action after adapting to external stimuli) in the SRM circuit, showing V_{in}, V_{mem1}, V_{out}, V_{th}, and V_{ext}. **(c)** Voltage pulse waveforms for the function of lateral inhibition (signals from other neurons inhibit the generation of action) in the SRM circuit, showing V_{in}, V_{mem1}, V_{out}, V_{th}, and V_{ext}. **(d)** Hardware-software co-implementation SNN based on SRM for feature extraction, audio recognition, and application.

Data availability

All data needed to support the conclusions in the paper are presented in the manuscript and/or the Electronic Supplementary Material. Additional data related to this paper may be requested from the corresponding author upon request.

Acknowledgements

This project was supervised and directed by M.X. P.P. and M.X. conceived this work. P.P. and M.X. designed the experiments. P.P. and R.O. conducted the device fabrication and the electrical measurements. P.P. performed the material characterization. J.H. conducted the neural network simulation. X.F. designed the circuits. Other authors provided and preprocessed materials. All authors contributed to the discussion and results analysis. P.P. wrote and M.X. revised the manuscript. This work was partially conducted in the Microelectronics Process and Device Laboratory at the School of Microelectronics Science and Technology, Sun Yat-sen University. This work is supported by the National Natural Science Foundation of China (62504258) and the overseas postdoc talent funding by the Ministry of Education, China.

Use of AI statement

None.

References

[1] Zidan, M. A.; Strachan, J. P.; Lu, W. D. The future of electronics based on memristive systems. *Nat. Electron.* **2018**, *1*, 22-29.

[2] Liu, A.; Zhang, X.; Liu, Z.; Li, Y.; Peng, X.; Li, X.; Qin, Y.; Hu, C.; Qiu, Y.; Jiang, H.; Wang, Y.; Li, Y.; Tang, J.; Liu, J.; Guo, H.; Deng, T.; Peng, S.; Tian, H.; Ren, T. The roadmap of 2D materials and devices toward chips. *Nano-Micro Lett.* **2024**, *16*, 119-196.

[3] Sun, W.; Gao, B.; Chi, M.; Xia, Q.; Yang, J. J.; Qian, H.; Wu, H. Understanding memristive switching via in situ characterization and device modeling. *Nat. Commun.* **2019**, *10*, 3453.

[4] Choi, S.; Yang, J.; Wang, G. Emerging memristive artificial synapses and neurons for energy‐efficient neuromorphic computing. *Adv. Mater.* **2020**, *32*, 2004659.

[5] Duan, X.; Cao, Z.; Gao, K.; Yan, W.; Sun, S.; Zhou, G.; Wu, Z.; Ren, F.; Sun, B. Memristor‐based neuromorphic chips. *Adv. Mater.* **2024**, *36*, 2310704.

[6] Chen, J.; Wang, W.; Yan, X. Two-dimensional material-based devices for in-sensor computing. *npj Unconventional Computing* **2025**, *2*, 19.

[7] Lin, Z.; Liu, Y.; Halim, U.; Ding, M.; Liu, Y.; Wang, Y.; Jia, C.; Chen, P.; Duan, X.; Wang, C. Solution-processable 2D semiconductors for high-performance large-area electronics. *Nature* **2018**, *562*, 254-258.

[8] Ippolito, S.; Kelly, A. G.; Furlan De Oliveira, R.; Stoeckel, M.; Iglesias, D.; Roy, A.; Downing, C.; Bian, Z.; Lombardi, L.; Samad, Y. A.; Nicolosi, V.; Ferrari, A. C.; Coleman, J. N.; Samorì, P. Covalently interconnected transition metal dichalcogenide networks via defect engineering for high-performance electronic devices. *Nat. Nanotechnol.* **2021**, *16*, 592-598.

[9] Lin, Z.; He, Q.; Yin, A.; Xu, Y.; Wang, C.; Ding, M.; Cheng, H.; Papandrea, B.; Huang, Y.; Duan, X. Cosolvent approach for solution-processable electronic thin films. *ACS Nano* **2015**, *9*, 4398-4405.

[10] Liu, Z.; Wang, Y.; Zhang, Y.; Sun, S.; Zhang, T.; Zeng, Y. J.; Hu, L.; Zhuge, F.; Lu, B.; Pan, X.; Ye, Z. Harnessing defects in SnSe film via photo‐induced doping for fully light‐controlled artificial synapse. *Adv. Mater.* **2024**, *37*, 2410783.

[11] Kim, J.; Rhee, D.; Jung, M.; Cheon, G. J.; Kim, K.; Kim, J. H.; Park, J. Y.; Yoon, J.; Lim, D. U.; Cho, J. H.; Kim, I. S.; Son, D.; Jariwala, D.; Kang, J. Defect-engineered semiconducting van der Waals thin film at metal–semiconductor interface of field-effect transistors. *ACS Nano* **2024**, *18*, 1073-1083.

[12] Zhang, W.; Gao, H.; Deng, C.; Lv, T.; Hu, S.; Wu, H.; Xue, S.; Tao, Y.; Deng, L.; Xiong, W. An ultrathin memristor based on a two-dimensional WS$_2$/MoS$_2$ heterojunction. *Nanoscale* **2021**, *13*, 11497-11504.

[13] Peng, Y.; Cui, C.; Li, L.; Wang, Y.; Wang, Q.; Tian, J.; Huang, Z.; Huang, B.; Zhang, Y.; Li, X.; Tang, J.; Chu, Y.; Yang, W.; Shi, D.; Du, L.; Li, N.; Zhang, G. Medium-scale flexible integrated circuits based on 2D semiconductors. *Nat. Commun.* **2024**, *15*, 10833.

[14] Huang, X.; Tong, L.; Xu, L.; Shi, W.; Peng, Z.; Li, Z.; Yu, X.; Li, W.; Wang, Y.; Zhang, X.; Gong, X.; Xu, J.; Qiu, X.; Wen, H.; Wang, J.; Hu, X.; Xiong, C.; Ye, Y.; Miao, X.; Ye, L. 2D MoS$_2$-based reconfigurable analog hardware. *Nat. Commun.* **2025**, *16*, 101.

[15] Ao, M.; Zhou, X.; Kong, X.; Gou, S.; Chen, S.; Dong, X.; Zhu, Y.; Sun, Q.; Zhang, Z.; Zhang, J.; Zhang, Q.; Hu, Y.; Sheng, C.; Wang, K.; Wang, S.; Wan, J.; Han, J.; Bao, W.; Zhou, P. A RISC-V 32-bit microprocessor based on two-dimensional semiconductors. *Nature* **2025**, *640*, 654-661.

[16] Mei, T.; Chen, F.; Huang, T.; Feng, Z.; Wan, T.; Han, Z.; Li, Z.; Hu, L.; Lin, C.; Lu, Y.; Cheng, W.; Qi, D.; Chu, D. Ion–electron interactions in 2D nanomaterials-based artificial synapses for neuromorphic applications. *ACS Nano* **2025**, *19*, 17140-17172.

[17] Ghuman, K. K.; Yadav, S.; Singh, C. V. Adsorption and dissociation of H_2O on monolayered MoS$_2$ edges: energetics and mechanism from *ab Initio* Simulations. *The Journal of Physical Chemistry C* **2015**, *119*, 6518-6529.

[18] Zhou, W.; Zou, X.; Najmaei, S.; Liu, Z.; Shi, Y.; Kong, J.; Lou, J.; Ajayan, P. M.; Yakobson, B. I.; Idrobo, J. Intrinsic structural defects in monolayer molybdenum disulfide. *Nano Lett.* **2013**, *13*, 2615-2622.

[19] Abnavi, A.; Ahmadi, R.; Hasani, A.; Fawzy, M.; Mohammadzadeh, M. R.; De Silva, T.; Yu, N.; Adachi, M. M. Free-standing multilayer molybdenum disulfide memristor for brain-inspired neuromorphic applications. *ACS Appl. Mater.*

Interfaces **2021**, *13*, 45843-45853.

[20] Son, D.; Chae, S. I.; Kim, M.; Choi, M. K.; Yang, J.; Park, K.; Kale, V. S.; Koo, J. H.; Choi, C.; Lee, M. Colloidal synthesis of uniform‐sized molybdenum disulfide nanosheets for wafer‐scale flexible nonvolatile memory. *Adv. Mater.* **2016**, *28*, 9326-9332.

[21] Wang, M.; Cai, S.; Pan, C.; Wang, C.; Lian, X.; Zhuo, Y.; Xu, K.; Cao, T.; Pan, X.; Wang, B.; Liang, S.; Yang, J. J.; Wang, P.; Miao, F. Robust memristors based on layered two-dimensional materials. *Nat. Electron.* **2018**, *1*, 130-136.

[22] Shao, G.; Xu, J.; Gao, S.; Zhang, Z.; Liu, S.; Zhang, X.; Zhou, Z. Unsaturated bi‐heterometal clusters in metal‐vacancy sites of 2D MoS$_2$ for efficient hydrogen evolution. *Carbon Energy* **2024**, *6*, e417.

[23] Lee, E.; Kim, J.; Park, J.; Hwang, J.; Jang, H.; Cho, K.; Choi, W. Realizing electronic synapses by defect engineering in polycrystalline two-dimensional MoS$_2$ for neuromorphic computing. *ACS Appl. Mater. Interfaces* **2023**, *15*, 15839-15847.

[24] Saha, P.; Sahad E, M.; Sathyanarayana, S.; Das, B. C. Solution-processed robust multifunctional memristor of 2D layered material thin film. *ACS Nano* **2024**, *18*, 1137-1148.

[25] Li, D.; Wu, B.; Zhu, X.; Wang, J.; Ryu, B.; Lu, W. D.; Lu, W.; Liang, X. MoS$_2$ memristors exhibiting variable switching characteristics toward biorealistic synaptic emulation. *ACS Nano* **2018**, *12*, 9240-9252.

[26] Liu, X.; Wang, S.; Di, Z.; Wu, H.; Liu, C.; Zhou, P. An optoelectronic synapse based on two‐dimensional violet phosphorus heterostructure. *Adv. Sci.* **2023**, *10*, 2301851.

[27] Tang, B.; Veluri, H.; Li, Y.; Yu, Z. G.; Waqar, M.; Leong, J. F.; Sivan, M.; Zamburg, E.; Zhang, Y.; Wang, J.; Thean, A. V. Wafer-scale solution-processed 2D material analog resistive memory array for memory-based computing. *Nat. Commun.* **2022**, *13*, 3037.

[28] Sangwan, V. K.; Rangnekar, S. V.; Kang, J.; Shen, J.; Lee, H. S.; Lam, D.; Shen, J.; Liu, X.; Moraes, A. C. M.; Kuo, L.; Gu, J.; Wang, H.; Hersam, M. C. Visualizing thermally activated memristive switching in percolating networks of solution‐processed 2D semiconductors. *Adv. Funct. Mater.* **2021**, *31*, 2107385.

[29] Dragoman, M.; Dragoman, D. Negative differential resistance in novel nanoscale devices. *Solid-State Electron.* **2022**, *197*, 108464.

[30] Xiao, M.; Shen, D.; Musselman, K. P.; Duley, W. W.; Zhou, Y. N. Oxygen vacancy migration/diffusion induced synaptic plasticity in a single titanate nanobelt. *Nanoscale* **2018**, *10*, 6069-6079.

[31] Shim, S.; Kim, S.; Lee, D.; Kim, H.; Kwon, M. J.; Cho, S. Y.; Lestari, W. A.; Seo, J.; Yeo, D.; Na, J.; Kundale, S. S.; Oh, N.; Park, J. H. Infrared‐triggered retinomorphic artificial synapse electronic device containing multi‐dimensional van der Waals heterojunctions. *Small* **2025**, *21*, 2410892.

[32] Cheng, J.; Zhang, P.; Ouyang, X.; Tang, W.; Song, B.; Zhang, Y.; Zheng, Y.; Pan, A. 2D memory enabled by electrical stimulation‐induced defect engineering for complicated neuromorphic computing. *Adv. Funct. Mater.* **2025**, *35*.

[33] Peng, Z.; Grillo, A.; Pelella, A.; Liu, X.; Boyes, M.; Xiao, X.; Zhao, M.; Wang, J.; Hu, Z.; Bartolomeo, A. D.; Casiraghi, C. Fully printed memristors made with MoS$_2$ and graphene water-based inks. *Mater. Horiz.* **2024**, *11*, 1344-1353.

[34] Varshney, K.; Shukla, P.; Prakash, B.; Das, D. M.; Rawat, B. Enhancing resistive switching characteristics of MoS$_2$-based memristor through O$_2$ plasma irradiation-induced defects. *IEEE J. Electron Devices Soc.* **2024**, *13*, 737-744.

[35] Ding, K.; Wang, J.; Zhou, Y.; Tian, H.; Lu, L.; Mazzarello, R.; Jia, C.; Zhang, W.; Rao, F.; Ma, E. Phase-change heterostructure enables ultralow noise and drift for memory operation. *Science* **2019**, *366*, 210-215.

[36] Xiao, M.; Hellenbrand, M.; Strkalj, N.; Bakhit, B.; Sun, Z.; Barmpatsalos, N.; Joksas, D.; Dou, H.; Hu, Z.; Lu, P.; Karki, S.; Kunwar, S.; Major, J. D.; Chen, A.; Wang, H.; Jia, Q.; Mehonic, A.; MacManus Driscoll, J. L. Ultra‐fast non‐volatile resistive switching devices with over 512 distinct and stable levels for memory and neuromorphic computing. *Adv. Funct. Mater.* **2025**, *35*, 2418980.

[37] Wu, Q.; Luo, Y.; Xie, R.; Nong, H.; Cai, Z.; Tang, L.; Tan, J.; Feng, S.; Zhao, S.; Yu, Q.; Lin, J.; Chai, G.; Liu, B. Space‐confined one‐step growth of 2D MoO$_2$/MoS$_2$ vertical heterostructures for superior hydrogen evolution in alkaline electrolytes. *Small* **2022**, *18*, 2201051.

[38] Xiong, X.; Wu, F.; Ouyang, Y.; Liu, Y.; Wang, Z.; Tian, H.; Dong, M. Oxygen incorporated MoS$_2$ for rectification‐mediated resistive switching and artificial neural network. *Adv. Funct. Mater.* **2024**, *34*, 2213348.

[39] Aryeetey, F.; Ignatova, T.; Aravamudhan, S. Quantification of defects engineered in single layer MoS$_2$. *RSC Adv.* **2020**, *10*, 22996-23001.

[40] Li, H.; Zhang, Q.; Yap, C. C. R.; Tay, B. K.; Edwin, T. H. T.; Olivier, A.; Baillargeat, D. From Bulk to Monolayer MoS$_2$: evolution of Raman scattering. *Adv. Funct. Mater.* **2012**, *22*, 1385-1390.

[41] Parkin, W. M.; Balan, A.; Liang, L.; Das, P. M.; Lamparski, M.; Naylor, C. H.; Rodríguez-Manzo, J. A.; Johnson, A. T. C.; Meunier, V.; Drndić, M. Raman shifts in electron-irradiated monolayer MoS$_2$. *ACS Nano* **2016**, *10*, 4134-4142.

[42] Kim, H.; Son, J.; Kulkarni, A.; Ahn, C.; Kim, K. S.; Shin, D.; Yeom, G. Y.; Kim, T. Highly uniform wafer-scale synthesis of alpha-MoO$_3$ by plasma enhanced chemical vapor deposition. *Nanotechnology* **2017**, *28*, 175601.

[43] Thorat, A.; Tikote, K.; Bhadane, M.; Phatangare, A.; Bhoraskar, V.; Dhole, S.; Dahiwale, S. Effect of low energy nitrogen ion irradiation on MoO$_3$ films. *Opt. Mater.* **2022**, *128*, 112349.

[44] Guo, Y.; Robertson, J. Origin of the high work function and high conductivity of MoO$_3$. *Appl. Phys. Lett.* **2014**, *105*, 222110.

[45] Zhang, C.; Jiang, L.; Zhang, Y.; Hu, J.; Leung, M. K. H. Janus effect of O_2 plasma modification on the electrocatalytic hydrogen evolution reaction of MoS_2. *J. Catal.* **2018**, *361*, 384-392.

[46] Sunu, S. S.; Prabhu, E.; Jayaraman, V.; Gnanasekar, K. I.; Seshagiri, T. K.; Gnanasekaran, T. Electrical conductivity and gas sensing properties of MoO_3. *Sensors and Actuators B: Chemical* **2004**, *101*, 161-174.

[47] Coy Diaz, H.; Addou, R.; Batzill, M. Interface properties of CVD grown graphene transferred onto MoS_2 (0001). *Nanoscale* **2014**, *6*, 1071-1078.

[48] Donarelli, M.; Bisti, F.; Perrozzi, F.; Ottaviano, L. Tunable sulfur desorption in exfoliated MoS_2 by means of thermal annealing in ultra-high vacuum. *Chem. Phys. Lett.* **2013**, *588*, 198-202.

[49] Kim, C.; Moon, I.; Lee, D.; Choi, M. S.; Ahmed, F.; Nam, S.; Cho, Y.; Shin, H.; Park, S.; Yoo, W. J. Fermi level pinning at electrical metal contacts of monolayer molybdenum dichalcogenides. *ACS Nano* **2017**, *11*, 1588-1596.

[50] Zhang, W.; Gao, B.; Tang, J.; Yao, P.; Yu, S.; Chang, M.; Yoo, H.; Qian, H.; Wu, H. Neuro-inspired computing chips. *Nat. Electron.* **2020**, *3*, 371-382.

[51] Tang, X.; Ma, X.; Ha, S.; Sun, W.; He, N.; Xue, S.; Cai, G.; Zhao, J. S. Solution-processed SnO_2/SnS_2 bilayer-based robust memristors for reliable neuromorphic computing. *Nanoscale Horiz.* **2026**, *10*, 1039.

[52] She, Y.; Wang, F.; Zhao, X.; Zhang, Z.; Li, C.; Pan, H.; Hu, K.; Song, Z.; Zhang, K. Oxygen vacancy-dependent synaptic dynamic behavior of TiO_x-based transparent memristor. *IEEE Trans. Electron Devices* **2021**, *68*, 1950-1955.

[53] Park, J.; Jang, H.; Byun, Y.; Na, H.; Ji, H.; Kim, S. Improved memory and synaptic device performance of HfO_2-based multilayer memristor by inserting oxygen gradient TiO_x layer. *Chaos, Solitons & Fractals* **2025**, *191*, 115910.

[54] Feng, X.; Li, Y.; Wang, L.; Chen, S.; Yu, Z. G.; Tan, W. C.; Macadam, N.; Hu, G.; Huang, L.; Chen, L.; Gong, X.; Chi, D.; Hasan, T.; Thean, A. V. Y.; Zhang, Y. W.; Ang, K. W. A Fully Printed Flexible MoS_2 Memristive Artificial Synapse with Femtojoule Switching Energy. *Adv. Electron. Mater.* **2019**, *5*, 1900740.

[55] Bhattacharjee, S.; Caruso, E.; McEvoy, N.; Ó Coileáin, C.; O Neill, K.; Ansari, L.; Duesberg, G. S.; Nagle, R.; Cherkaoui, K.; Gity, F.; Hurley, P. K. Insights into multilevel resistive switching in monolayer MoS_2. *ACS Appl. Mater. Interfaces* **2020**, *12*, 6022-6029.

[56] Li, K.; Huang, M.; Wang, Y.; Tseng, Y.; Su, C. Wafer-scale fabrication of Al/MoS_2/Poly-Si memristors and insight of mechanism on the resistive switching. *ACS Appl. Electron. Mater.* **2024**, *6*, 777-784.

[57] Wang, Z.; Yan, X.; Hou, Q.; Liu, Y.; Zeng, X.; Kang, Y.; Zhao, W.; Li, X.; Yuan, S.; Qiu, R.; Uddin, M. H.; Wang, R.; Xia, Y.; Jian, M.; Kang, Y.; Gao, L.; Liang, S.; Liu, J. Z.; Wang, H.; Zhang, X. Scalable high yield exfoliation for monolayer nanosheets. *Nat. Commun.* **2023**, *14*.

[58] Shaban, A.; Bezugam, S. S.; Suri, M. An adaptive threshold neuron for recurrent spiking neural networks with nanodevice hardware implementation. *Nat. Commun.* **2021**, *12*, 4234.

[59] Yang, J.; Wang, R.; Wang, Z.; Ma, Q.; Mao, J.; Ren, Y.; Yang, X.; Zhou, Y.; Han, S. Leaky integrate-and-fire neurons based on perovskite memristor for spiking neural networks. *Nano Energy* **2020**, *74*, 104828.

[60] Wei, Q.; Tang, J.; Li, X.; Zhong, Y.; Gao, B.; Qian, H.; Wu, H. Artificial neuron with spike frequency adaptation based on Mott memristor. *2021 5th IEEE Electron Devices Technology &amp Manufacturing Conference (EDTM)* **2021**, 1-3.

[61] Huang, J.; Wang, T.; Huang, H.; Guo, X. Adaptive SRM neuron based on NbO_x memristive device for neuromorphic computing. *Chip* **2022**, *1*, 100015.

[62] Zhang, J.; Liu, G.; Yuan, J.; Liao, X.; Zhou, Y. Enhanced photoresponse in $PdSe_2$ via local plasma treatment: implication for advanced optoelectronic devices. *ACS Appl. Nano Mater.* **2025**, *8*, 3511-3518.

Electronic Supplementary Material

Sulfur/oxygen vacancy synergistic engineering in MoS_2-based neuromorphic devices

Pan Pan[1,2], Ruixiao Ou[1,2], Xiaolong Fan[1], Jianxian He[1], Siyi Wu[1], Chaogui Huang[1], Hasimuali Kanikai[1], Meila Peng[1], Xu Li[1], Javed Iqbal Saggu[3], and Ming Xiao[1,2,]

[1] *School of Microelectronics Science and Technology, Sun Yat-sen University, Zhuhai 519082, China*
[2] *Zhuhai Key Laboratory of Nano Sensing and Intelligent Detection, Zhuhai 519082, China*
[3] *Department of Physics, Quaid I Azam University, Islamabad 45320, Pakistan*

Supporting information to https://doi.org/10.26599/NR.2026.94908632

Address correspondence to xiaom37@mail.sysu.edu.cn

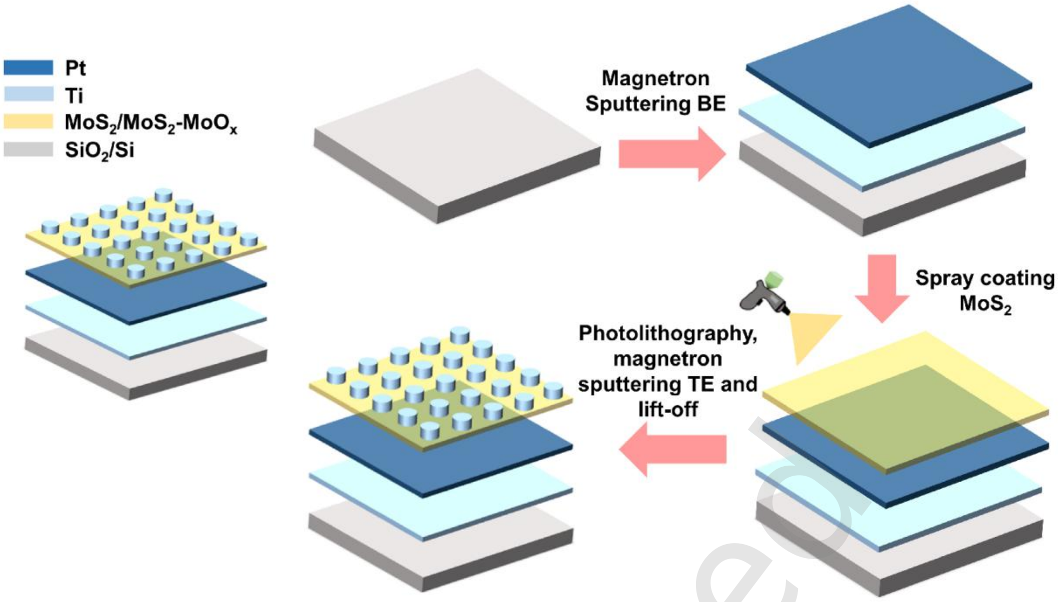

Figure S1. Schematic illustration of the device configuration and fabrication process.

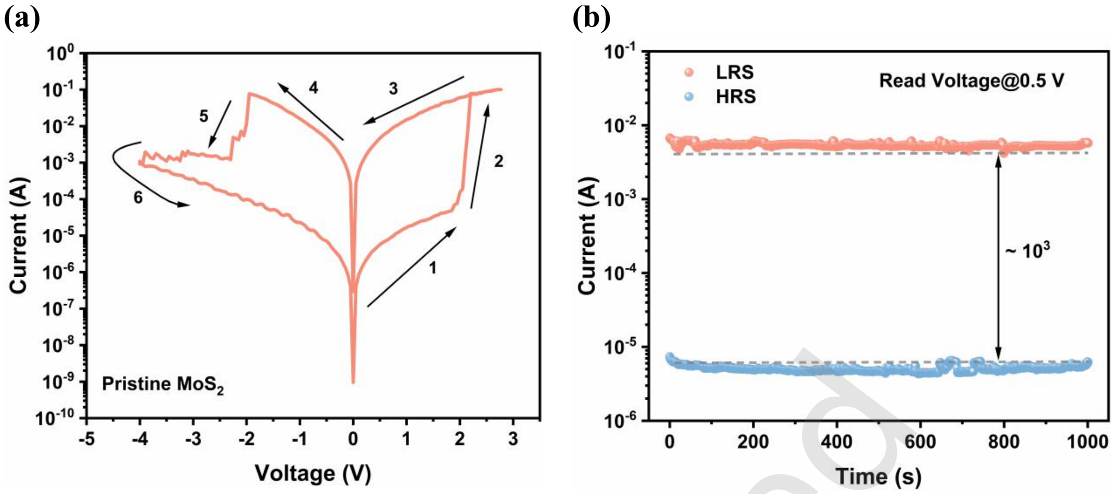

Figure S2. (a) The representative *I-V* curve of the pristine MoS$_2$ device. **(b)** Retention test of the pristine MoS$_2$ device, exceeding 1000 s.

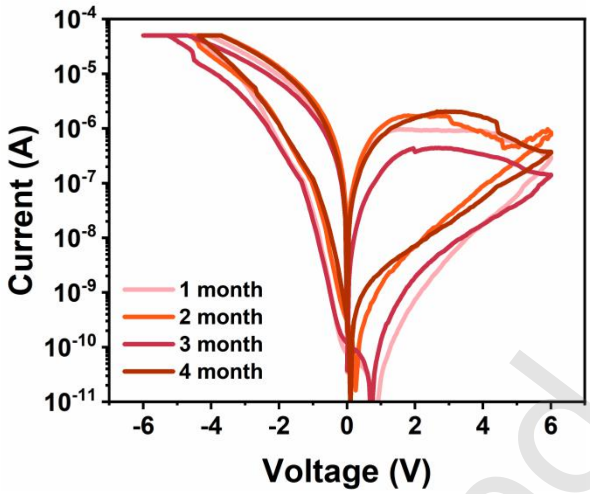

Figure S3. Long-term *I-V* stability of O-MoS_2.

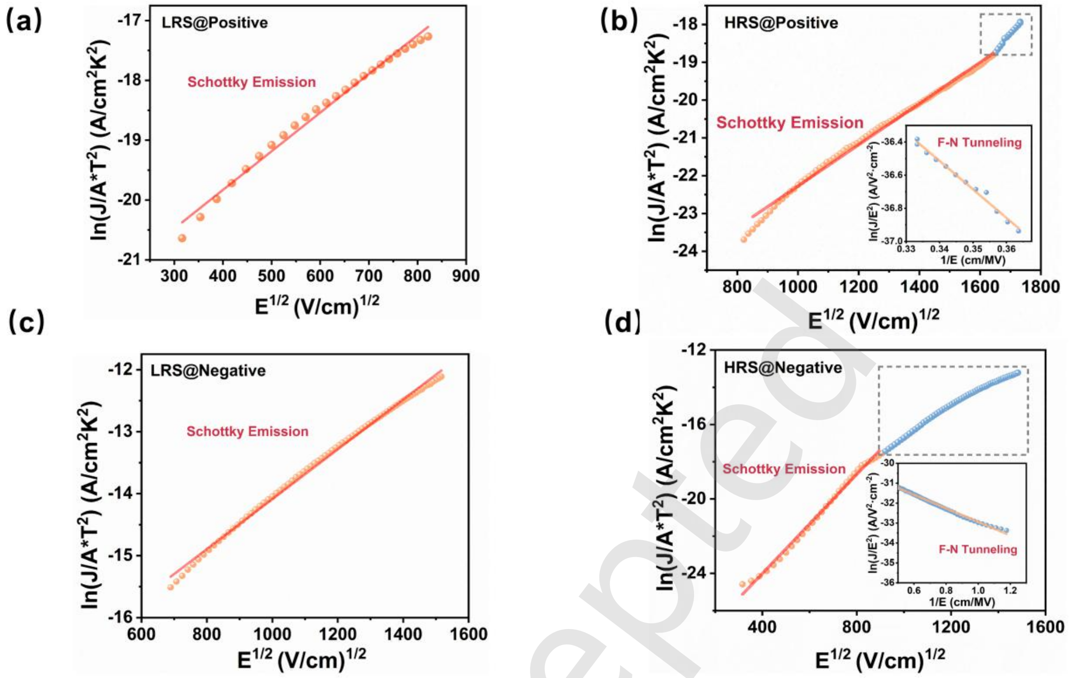

Figure S4. (a) Schottky emission fitting for LRS during positive DC voltage sweep. **(b)** Schottky emission model fitting for HRS during positive DC voltage sweep. **(c)** Schottky emission fitting for LRS during negative DC voltage sweeping. **(d)** Schottky emission and F-N tunnelling model fitting for HRS during positive DC voltage sweep.

At HRS during positive DC voltage sweeping, the *I-V* curve is fitted by a combined Schottky emission and F-N tunnelling model, while LRS during positive DC voltage sweeping is dominated by Schottky emission. Under low voltage conditions, Schottky emission dominates as the primary electron transport mechanism. Electrons with energies exceeding the barrier height overcome it via thermionic emission, contributing to the thermionic current. The Schottky emission function is expressed as follows:

$$J \propto AT^2 \exp\left[-q\left(\phi_b - \sqrt{qE/4\pi\varepsilon_0\varepsilon_r}\right)/KT\right] \quad (1)$$

Where J is the current density, T is the absolute temperature, q is the electronic charge, A is the effective Richardson constant, ϕ_b is the Schottky barrier height, K is the Boltzmann constant, E is the applied electric field, ε_0 is the vacuum permittivity, and ε_r is the optical dielectric constant. At HRS, a large number of V_O and V_S accumulate near the BE, which causes an enhancement of the Coulomb screening effect, leading to higher barriers. Consequently, the electron transport mechanism transforms into a combination of Schottky emission and F-N tunnelling (Under higher electric field). The F-N tunnelling formula is as follows:

$$J \propto V^2 \exp\left(\frac{-8\pi\left(2qm^*\right)^{1/2}}{3hV}\phi_b^{3/2}\right) \tag{2}$$

Where J is the current density, V is the applied voltage, q is the electronic charge, h is the Planck constant, ϕ_b is the Schottky barrier height, and m is the effective electron mass.

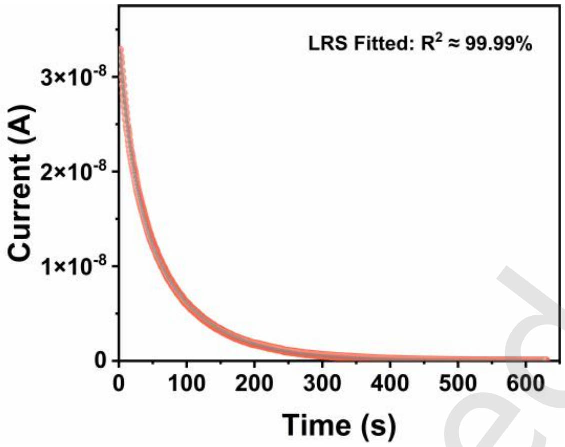

Figure S5. LRS current decay curve fitted with the double-exponential function of the volatile MoS_2-MoOx device. The fitted equation is as follows:

$$I(t) = I_0 + A_1 e^{t/\tau_1} + A_2 \mathrm{e}^{t/\tau_2}$$

Where I_0 is the steady-state residual current, A_1 and A_2 represent Amplitude coefficients of the fast and slow decay components, and τ_1 and τ_2 are characteristic time constants for each decay process. Here, τ_1 (20.67) corresponds to the rapid decay phase, potentially associated with adsorbed ions at the switching layer surface and defects exhibiting weak binding energies (e.g., shallow-level defects). Conversely, τ_2 (81.55) governs the slow decay phase, linked to carrier detrapping from deep-level defect centres with strong binding energies within the switching layer bulk.

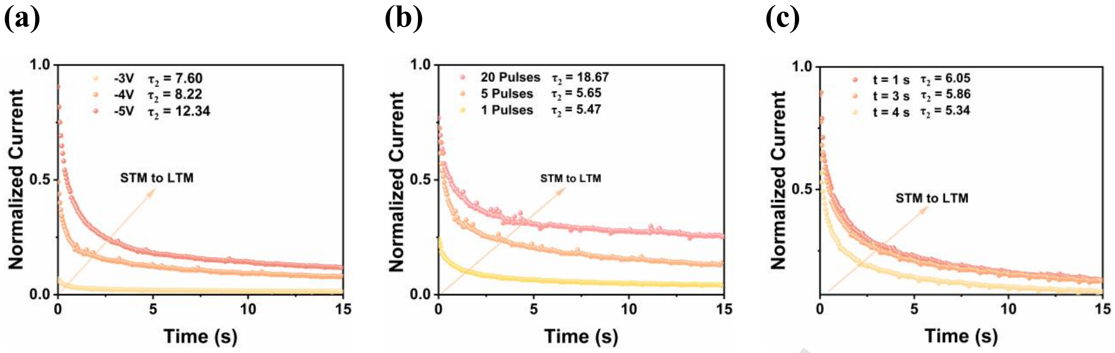

Figure S6. STM-to-LTM transition mediated by **(a)** voltage amplitude (-3 V, -4 V, and -5 V), **(b)** pulse number (1, 5, and 20), and **(c)** temporal interval (1 s, 3 s, and 4 s) modulation.

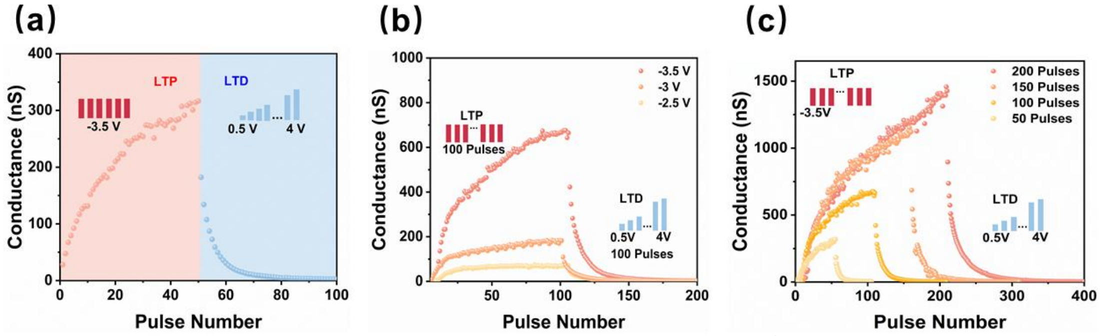

Figure S7. (a) LTP/LTD operation protocol: Fixed-amplitude pulses for LTP versus linear amplitude modulation (0.5 to 4 V) for LTD. **(b)** LTP/LTD characterisation under varied amplitudes (-2.5 V, -3V, and -3.5 V) and **(c)** pulse numbers (50, 100, 150, and 200).

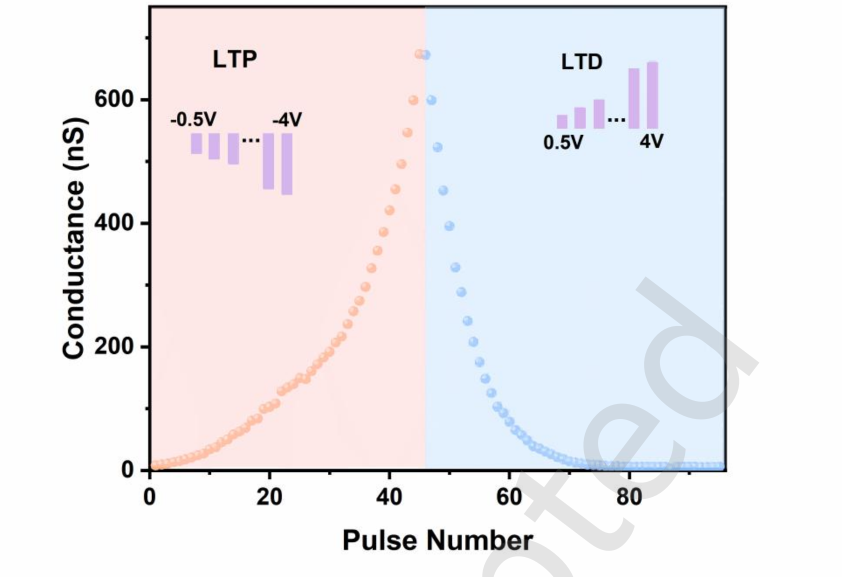

Figure S8. Second protocol of LTP/LTD operation. Voltage was applied using linear ramps from -0.5 V to -4 V for LTP and from 0.5 V to 4 V for LTD.

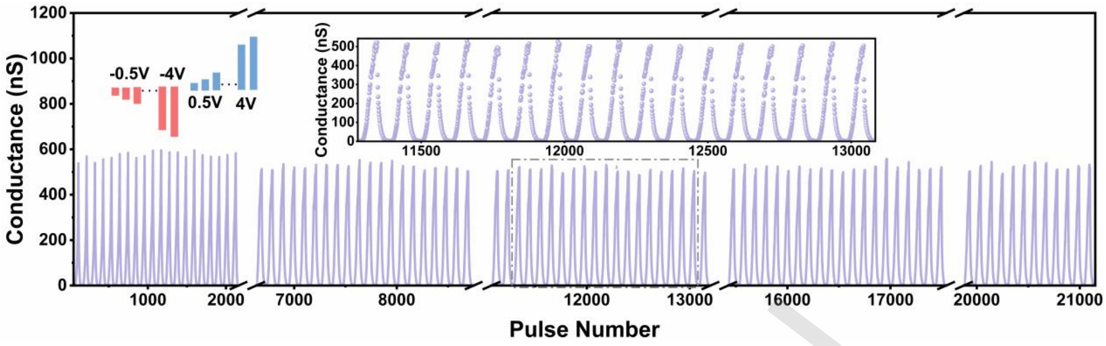

Figure S9. LTP/LTD cycling test exceeding 20000 voltage pulses. The LTP cycle-to-cycle variation is 20.36% and the LTD cycle-to-cycle variation is 12.77%.

Table S1: The LTP/LTD cycling test result comparison of MoS_2-based neuromorphic devices.

Structure	**Method**	**Defect modulation**	**G_{max}/G_{min}**	**Pulse number of LTP/LTD tests**	**Reference**
Ag/MoO_2-MoS_2/Ni/Au	CVD	Pristine defects	~3	600	2023[1]
Au/MoS_2/Au	CVD	Pristine defects	~7.7	650	2023[2]
Au/MoS_2/Au	PVD	Annealing and toluene treatment	~1.7	500	2023[3]
Au/MoS_2/Au	CVD	Ar plasma treatment	~1.85	400	2024[4]
TiN/MoS_xO_{2-x}/TiN	mechanical exfoliation	H_2O_2 treatment	~7.5	800	2024[5]
Au/Ti/MoS_2/Ti/Au	mechanical exfoliation	EBI and UVO treatment	~4.5	500	2024[6]
Au/MoS_2/AlO_x/Au	CVD	Pristine defects	~4	51200	2024[7]
Au/MoS_2-2D-PVK/Au	mechanical exfoliation	Pristine defects	~3	3000	2025[8]
Au/MoS_2/Au	mechanical exfoliation	Pristine defects	~1.15	400	2025[9]
Cu/MoS_2 QDs/ITO	Solution method	Pristine defects	~7	450	2025[10]
Ti/MoS_2-MoO_x/Pt	**Solution method**	**Naturally oxidized**	**~1200**	**10^5**	**This work**

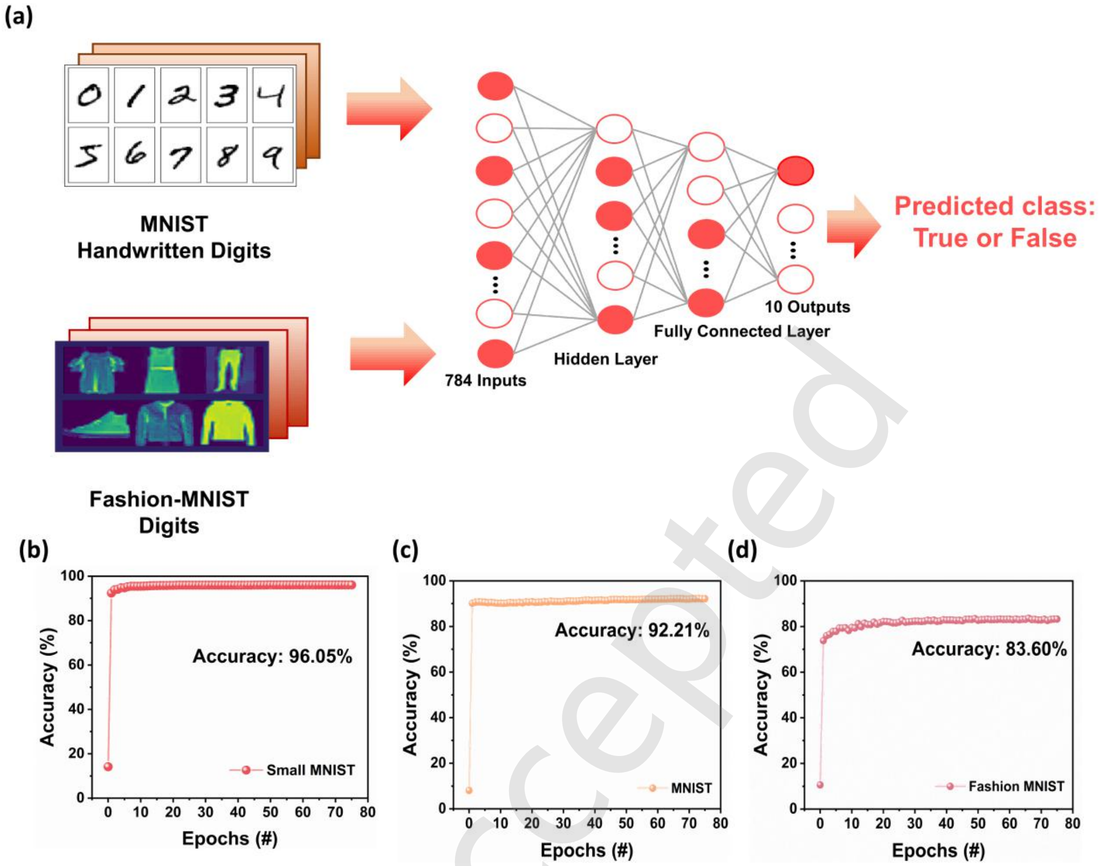

Figure S10. Simulation on a neural network. **(a)** Schematic of a neural network for MNIST/Fashion-MNIST pattern recognition stimulation. Pattern recognition stimulation accuracy curves for **(b)** Small MNIST, **(c)** MNIST, and **(d)** Fashion MNIST. The LTP/LTD data from **Figure S9** were used for the simulation.

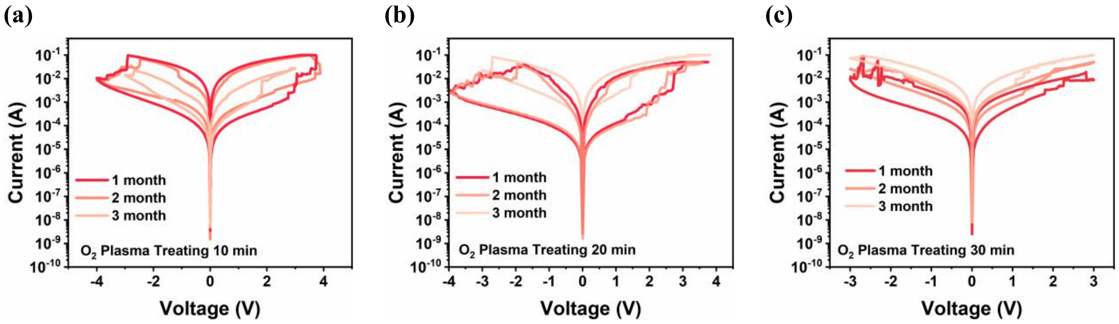

Figure S11. Long-term *I-V* stability of 10-MoS$_2$, 20-MoS$_2$, and 30-MoS$_2$.

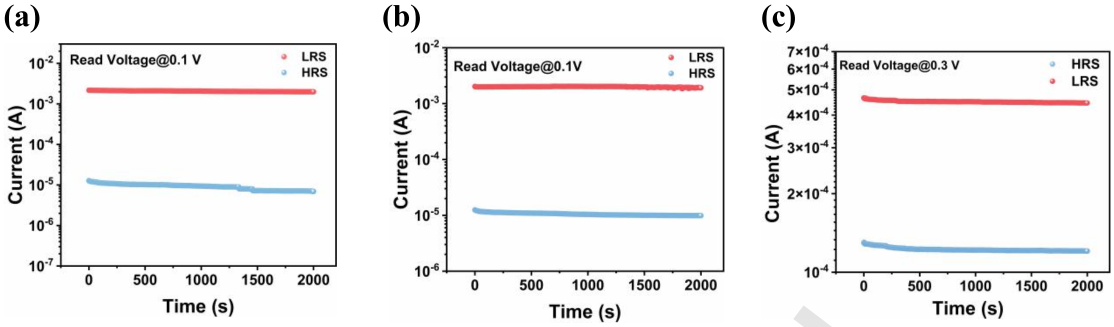

Figure S12. Retention tests of MoS_2-based devices treated with **(a)** 10, **(b)** 20, and **(c)** 30 min oxygen plasma over 2000 s.

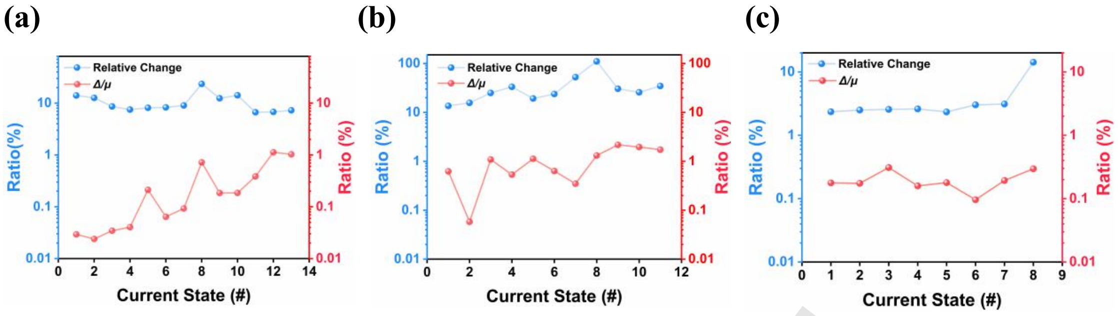

Figure S13. Change of *Δ/μ* ratios and relative change among two adjacent resistance states for each multilevel resistance state, **(a)** for the MoS_2 device with 10 min O_2 plasma treatment, **(b)** for the MoS_2 device with 20 min O_2 plasma treatment, and **(c)** for the MoS_2 device with 30 min O_2 plasma treatment

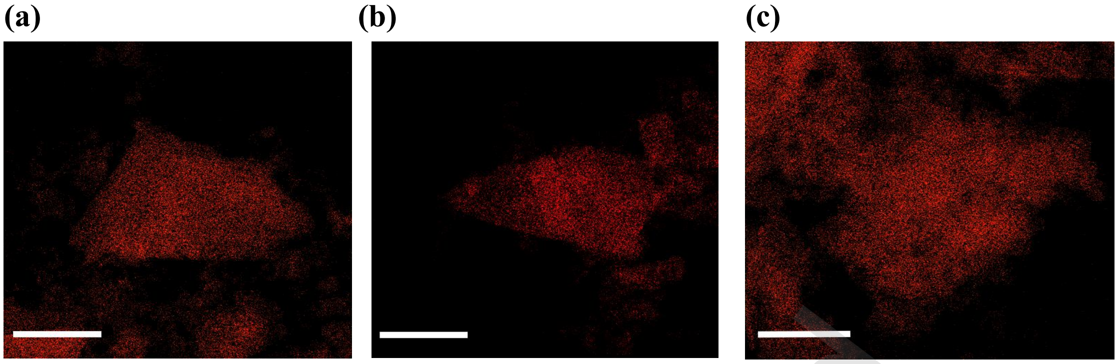

Figure S14. Molybdenum elemental mapping for **(a)** P-MoS_2, **(b)** O-MoS_2, and **(c)** plasma-MoS_2. The scale bar is 200 nm, 250 nm, and 200 nm, respectively. The Mo content in both P-MoS_2 and O-MoS_2 is approximately 33%, while that in plasma-MoS_2 decreases slightly to 31%, which may be attributed to the generation of Mo-related defects.

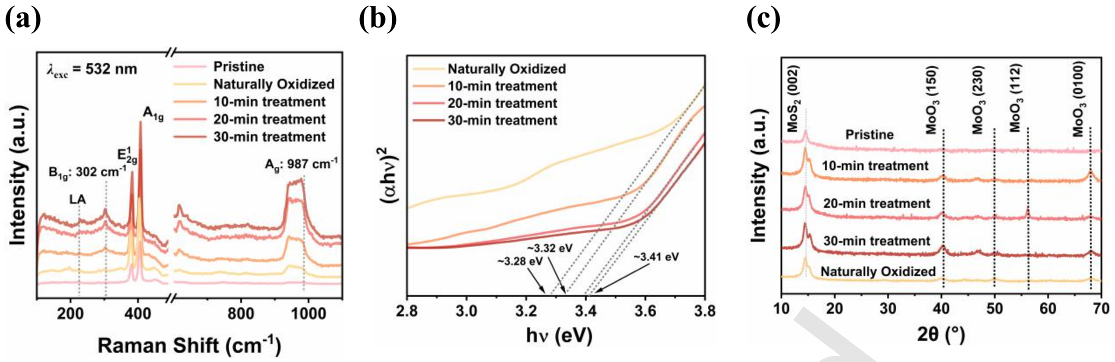

Figure S15. (a) Raman spectra of pristine-MoS_2, naturally-oxidized MoS_2-MoO_x, and plasma-treated MoS_2-MoO_x. E^1_{2g} and A_{1g} represent the typical mode of MoS_2. B_{1g} and A_g are the modes of MoO_3. The LA peak at about 226-227 cm^{-1} serves as an indicator of defect concentration, including V_S, Mo vacancies, and anti-site defects. **(b)** UV-vis results with prolonged O_2 plasma treatment, the value of E_g increased slightly. **(c)** XRD pattern characterisation demonstrates the presence of MoS_2 and MoO_3.

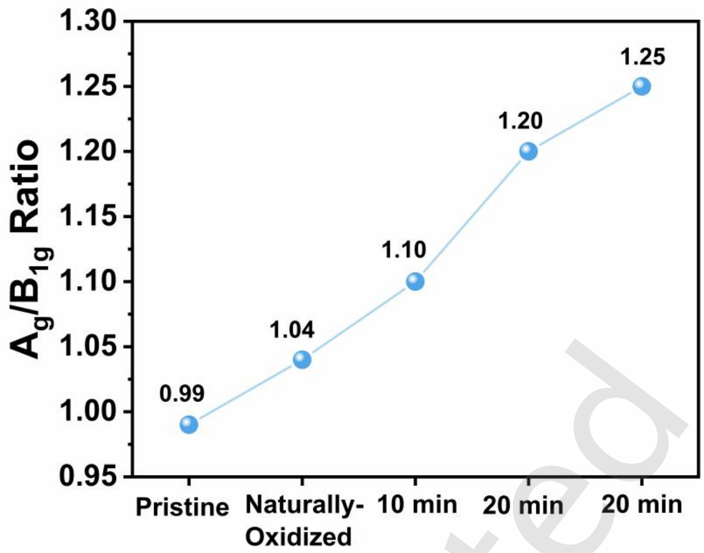

Figure S16. A_g/B_{1g} intensity ratio in Raman spectra of pristine, naturally-oxidized, and O_2 plasma-treated (10, 20, and 30 min) MoS_2-MoO_x samples. Monotonic increase likely due to progressive MoO_3 oxidation and defect generation.

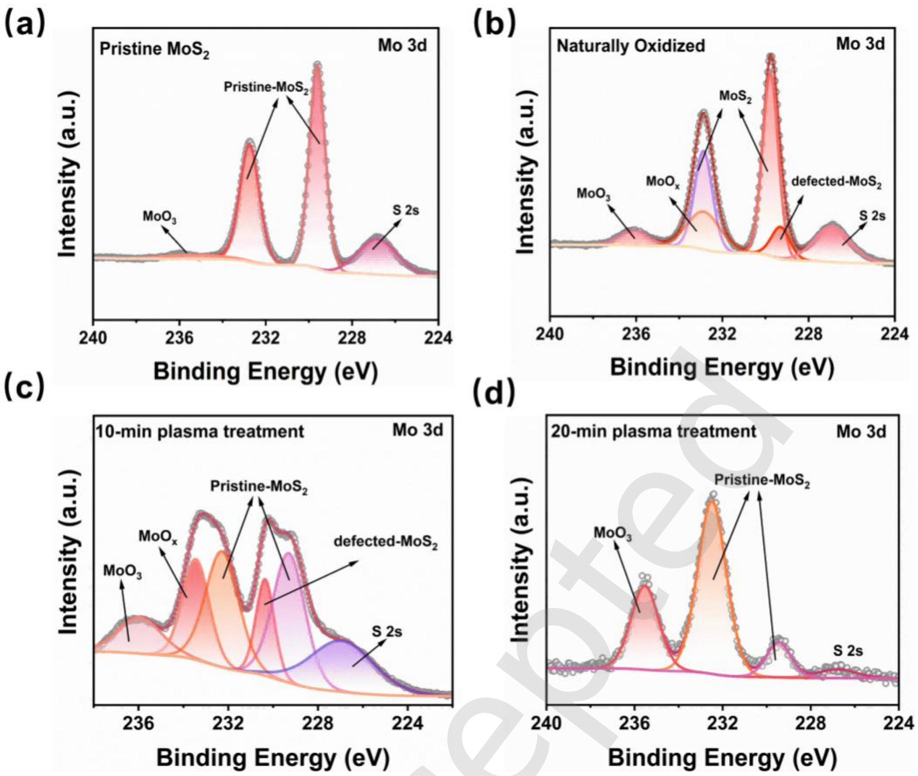

Figure S17. **(a)-(d)** Mo 3d XPS spectra of P-MoS$_2$, O-MoS$_2$, 10-MoS$_2$, and 20-MoS$_2$ samples, respectively. With increasing oxygen plasma treatment time, the contribution from defective-MoS$_2$ and suboxidic MoO$_x$ species decreases, while that of MoO$_3$ increases. P-MoS$_2$ exhibits characteristic MoS$_2$ XPS peaks. However, with progressive natural oxidation, the O-MoS$_2$ spectrum reveals the emergence of intermediate MoxSy species and oxidized MoO$_x$ components, accompanied by a more pronounced MoO$_3$ peak at ~236 eV. This indicates the transformation of MoS$_2$ into a mixed MoS$_2$-MoO$_x$ (and MoS$_{2\text{-}x}$O$_x$) phase. Compared to O-MoS$_2$, the 10-MoS$_2$ demonstrates a higher proportion of sub-stoichiometric MoO$_x$ and fully oxidized MoO$_3$, confirming continued surface oxidation induced by oxygen plasma. In the 20-MoS$_2$ spectrum, while distinct intermediate-phase signals are absent, a significant increase in the MoO$_3$ peak area further validates the persistence of this oxidation effect.

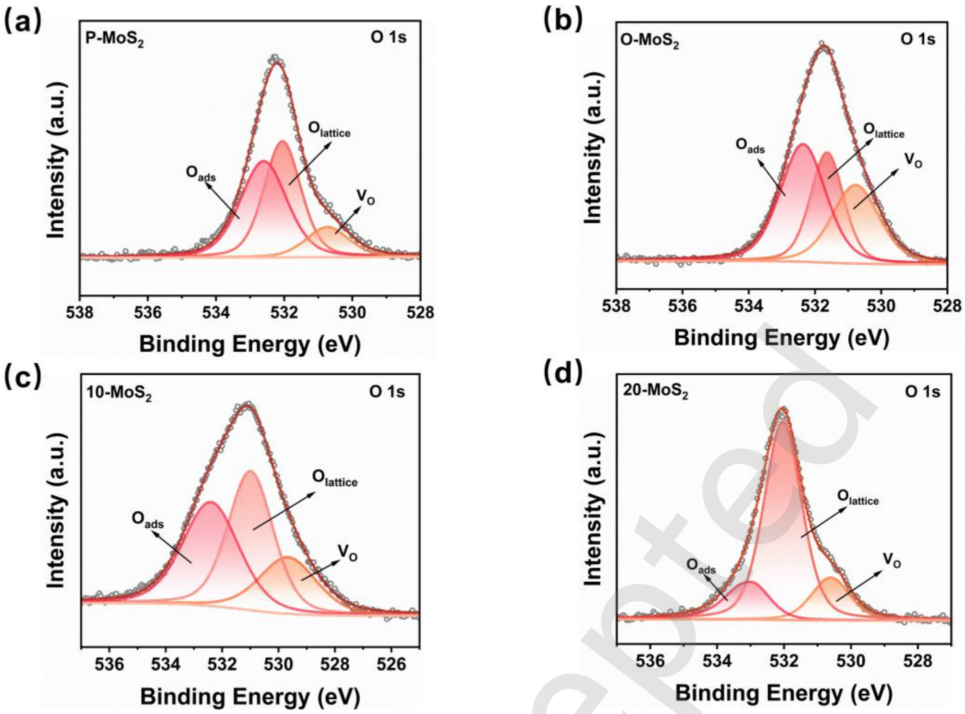

Figure S18. (a)-(d) O 3d XPS spectra of the P-MoS$_2$, O-MoS$_2$, 10-MoS$_2$ and 20-MoS$_2$ samples, respectively. As the oxidation process proceeds, the proportion of lattice oxygen increases, while the proportion of oxygen vacancies first increases and then decreases. The oxygen XPS spectra can be consistently deconvoluted into three characteristic peaks corresponding to lattice oxygen, adsorbed oxygen, and oxygen vacancies across all sample states[11]. From P-MoS2 to O-MoS$_2$ and plasma-treated MoS$_2$, lattice oxygen increases, adsorbed oxygen drops sharply in 20-MoS$_2$, and oxygen vacancies first rise then fall, indicating continuous oxidation converts oxygen vacancies and adsorbed oxygen to lattice oxygen.

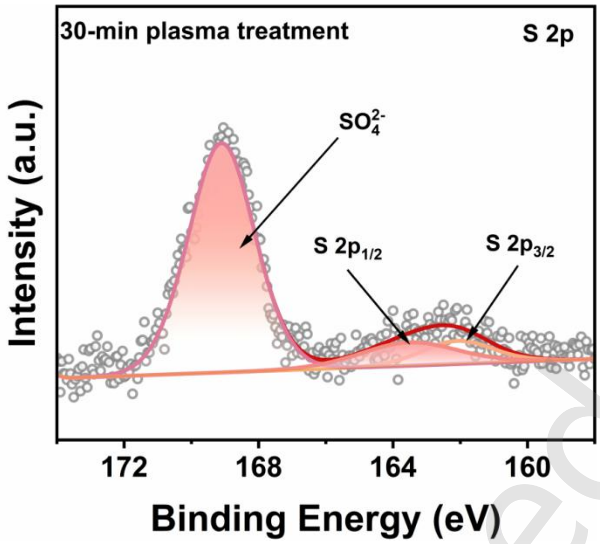

Figure S19. Sulfur XPS spectrum of the 30 min O_2 plasma-treated device. The deconvoluted peaks at approximately 169 eV, 163.9 eV, and 162 eV are assigned to the binding energies of SO_4^{2-}, S $2p_{1/2}$, and S $2p_{3/2}$, respectively.

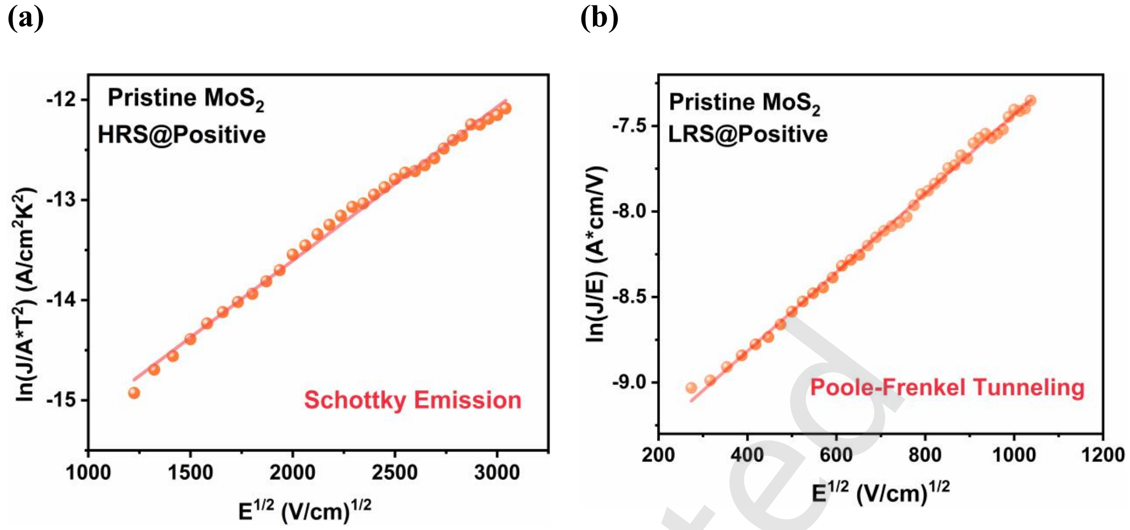

Figure S20. (a) Schottky emission fitting for P-MoS$_2$ in HRS ($R^2 \approx 99.5\%$) and **(b)** Poole-Frenkel tunnelling fitting for P-MoS$_2$ in LRS ($R^2 \approx 99.8\%$).

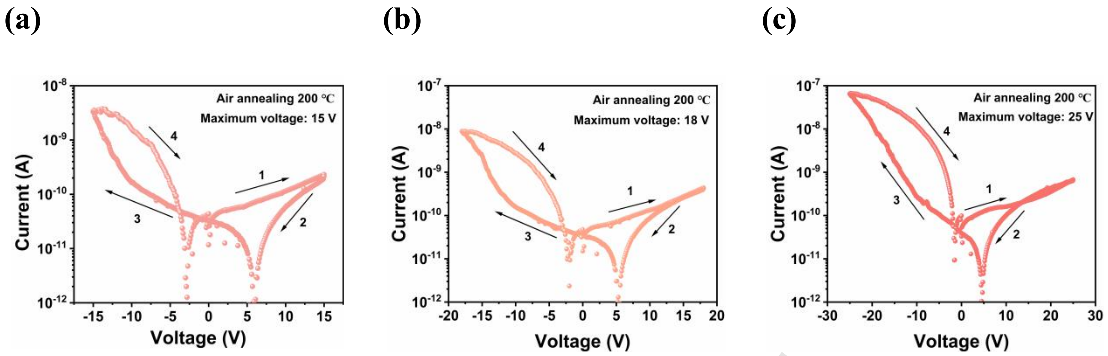

Figure S21. *I-V* curve of the MoS_2 device after 5 min annealing in a 200 ℃ atmosphere. SET/RESET voltage is **(a)** 15/-15V, **(b)** 18/-18 V, and **(c)** 25/-25 V. As the applied voltage increased, the device current level increased from 3×10^{-9} A to approximately 1×10^{-7}A. Rapid thermal annealing in ambient air induced the formation of a more insulating layer on the MoS_2 surface, resulting in lower current levels compared to O-MoS_2 counterparts.

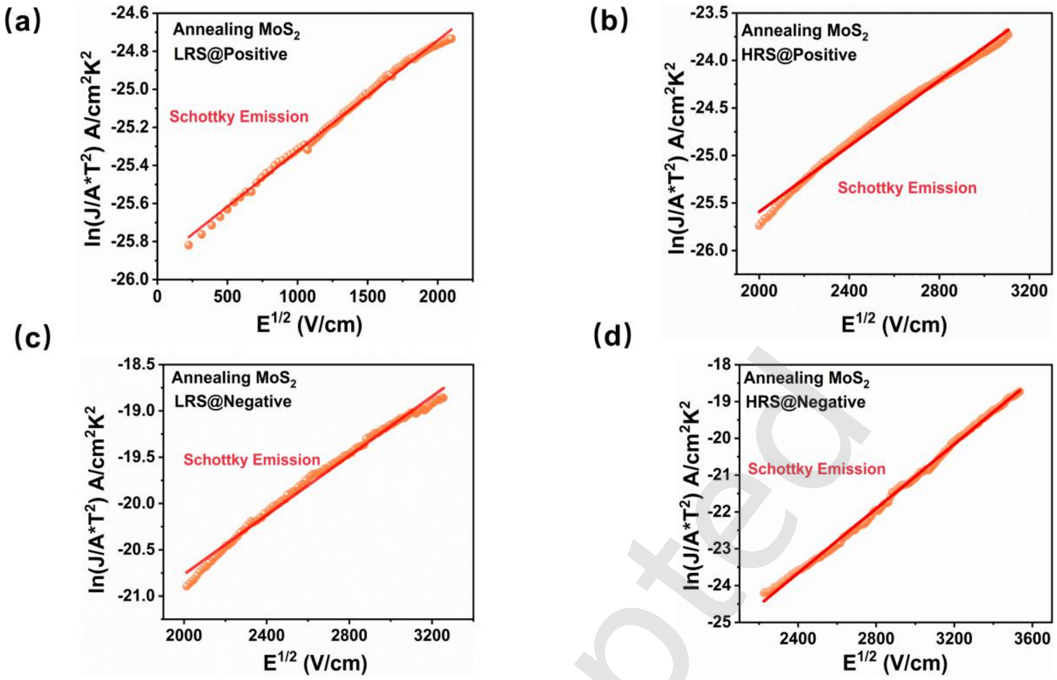

Figure S22. Fitting of the annealed MoS$_2$ device from **Fig. S17**c. Schottky emission fitting for **(a)** LRS during positive DC voltage sweep, **(b)** HRS during positive DC voltage sweep, **(c)** LRS, and **(d)** HRS during negative DC voltage sweep. Compared to the naturally-oxidized MoS$_2$ device, the Schottky barriers of HRS and LRS increased, which could be due to the formation of a more insulating layer and fewer in-plane defects.

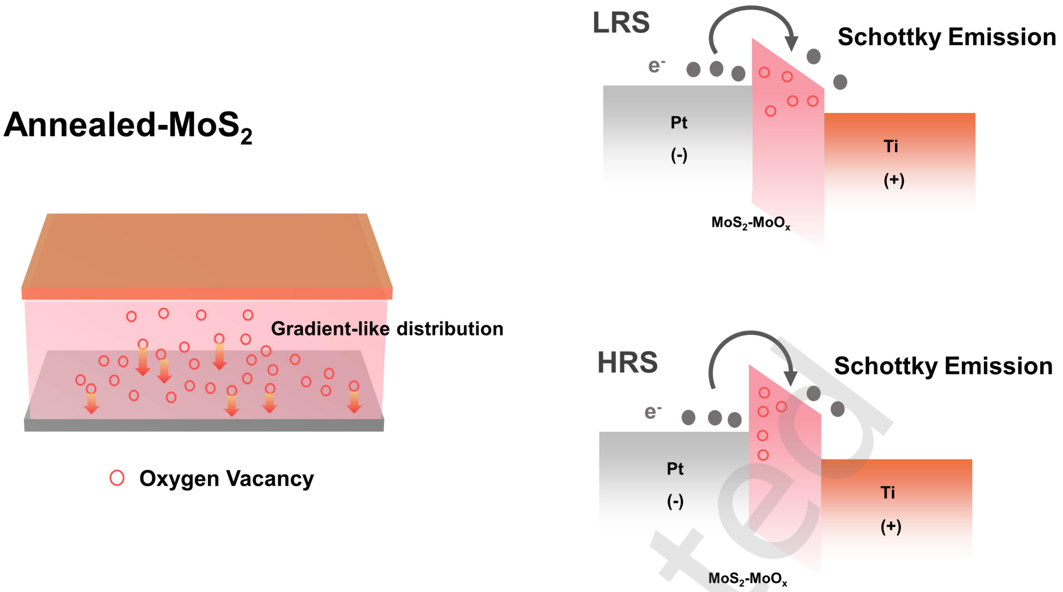

Figure S23. The energy band diagram of the annealed MoS$_2$. We speculate that as oxygen species occupy oxygen vacancy sites from top to bottom, oxygen vacancies in the switching layer of the annealed MoS$_2$ device exhibit a gradient distribution. This makes the region near the TE more insulating, while the region near the BE retains the original oxygen vacancy distribution. The operation mechanisms (global oxygen vacancy migration) and fitting models (Schottky emission) are similar to the O-MoS$_2$ device. .

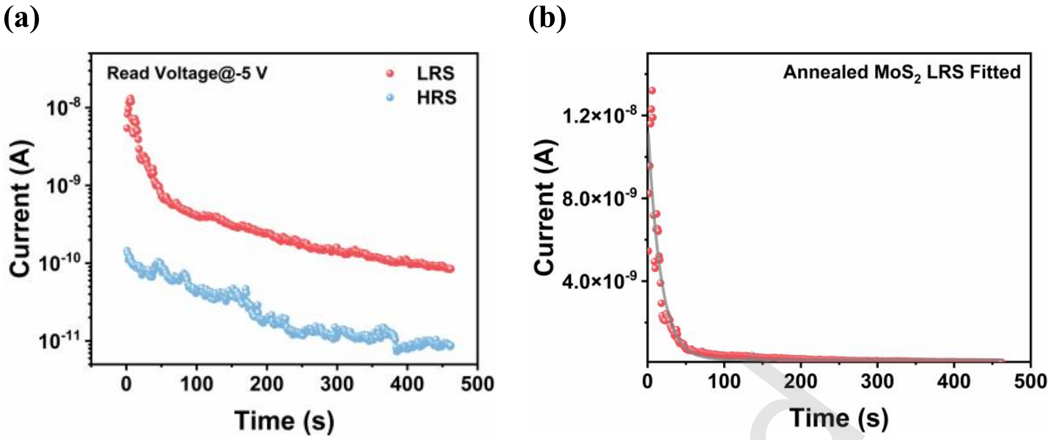

Figure S24. The retention of the annealed MoS_2 device. **(a)** Basic retention characteristics of the device. After 500 s, ILRS decays from 10-8A to 10-10 A while IHRS decreases from 10^{-10} A to 10^{-11} A. **(b)** The double exponential function fitting results for the LRS. Similar to the volatile characteristics observed in O-MoS_2, the volatile characteristics of annealed MoS_2 are likely associated with charge carrier trapping and detrapping processes. The value of τ_2 is 16.6, which is lower than that in O-MoS_2, and could be attributed to less shallow traps in the switching layer.

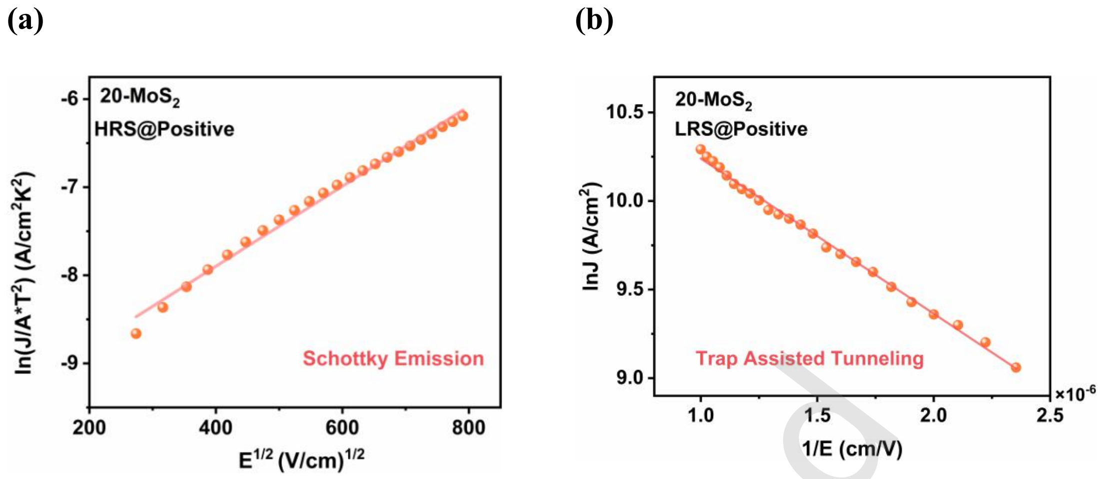

Figure S25. **(a)** Schottky emission fitting for 20-MoS_2 in HRS (R2 ≈ 98.5%) and **(b)** Trap-assisted tunnelling for 20-MoS_2 in LRS (R2 ≈ 98.8%) during positive DC voltage sweep.

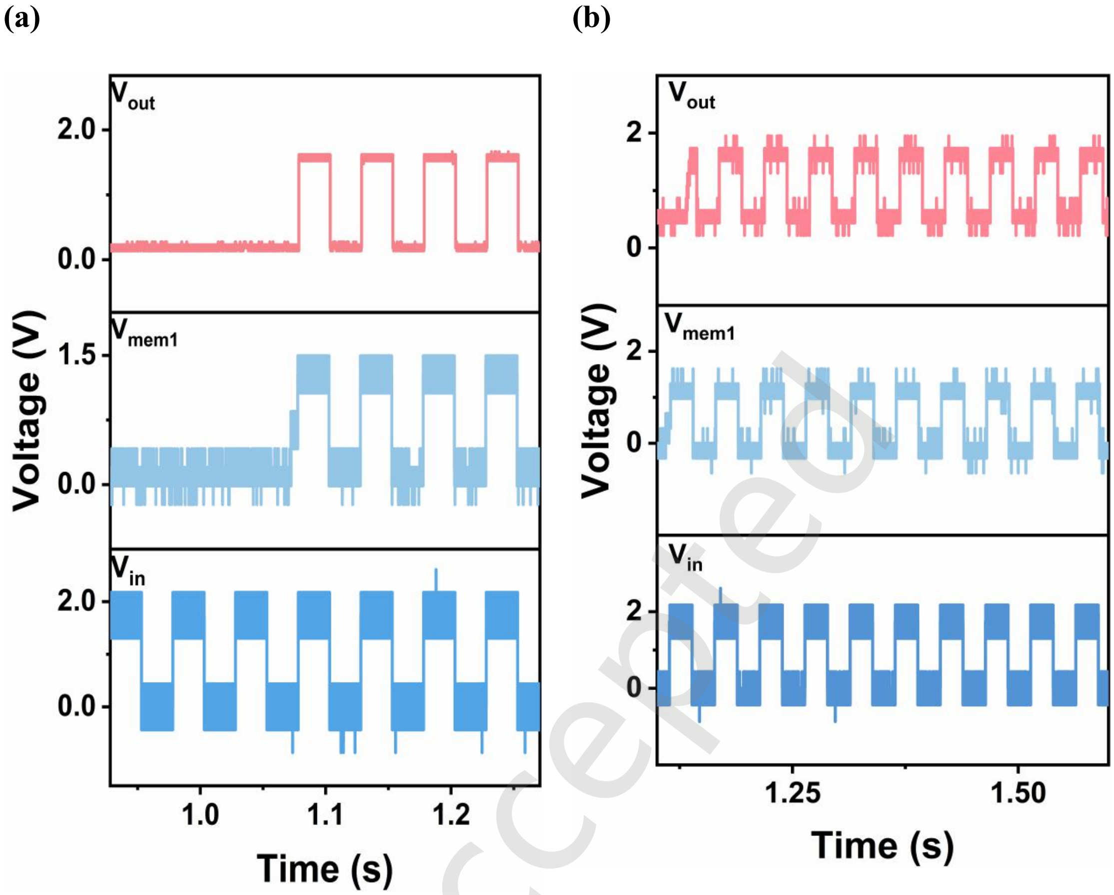

Figure S26. Basic function of the LIF module. **(a)** Fixed pulse amplitudes to emulate charge-accumulation-trigger and **(b)** fixed pulse amplitudes to emulate immediate trigger. Correspondingly, charge-accumulation-triggered firing emulates neuronal responses to less sensitive stimuli, while immediate firing responses occur in neurons to more sensitive stimuli.

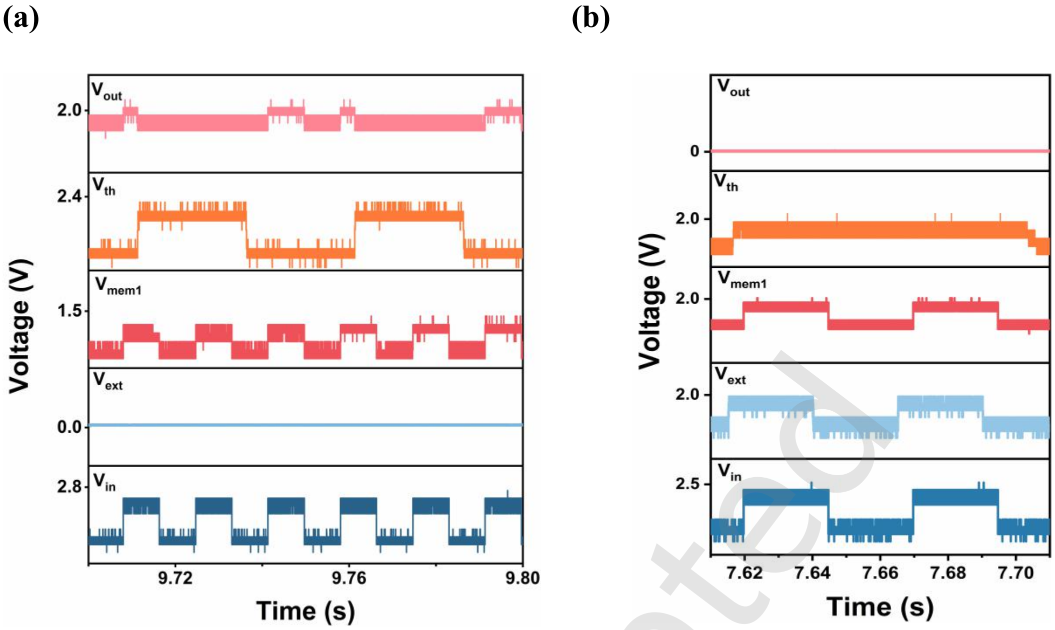

Figure S27. Waveforms of the SRM circuit with fixed input voltage pulse amplitudes, showing V_{in}, V_{mem1}, V_{th}, V_{out}, and V_{ext}, used to simulate **(a)** the neuronal refractory period and **(b)** the lateral inhibition function. Similar to the effects observed under stepwise-amplitude input pulses, the refractory period simulation demonstrates that an amplitude-fixed input pulse (V_{in}) elicits an output response (V_{out}), which subsequently elevates the threshold voltage (V_{th}), thereby suppressing further firing events. For lateral inhibition, signals from additional channels (V_{ext}) directly raise the threshold voltage, consequently inhibiting output generation.

References

[1] Yadav, R.; Poudyal, S.; Rajarapu, R.; Biswal, B.; Barman, P. K.; Kasiviswanathan, S.; Novoselov, K. S.; Misra, A. Low power volatile and nonvolatile memristive devices from 1D MoO$_2$ ‐ MoS$_2$ core–shell heterostructures for future bio‐inspired computing. *Small* **2024**, *20*, 2309163.

[2] Fu, S.; Park, J.; Gao, H.; Zhang, T.; Ji, X.; Fu, T.; Sun, L.; Kong, J.; Yao, J. Two-terminal MoS$_2$ memristor and the homogeneous integration with a MoS$_2$ Transistor for Neural Networks. *Nano Lett.* **2023**, *23*, 5869-5876.

[3] Lee, E.; Kim, J.; Park, J.; Hwang, J.; Jang, H.; Cho, K.; Choi, W. Realizing electronic synapses by defect engineering in polycrystalline two-dimensional MoS$_2$ for neuromorphic computing. *ACS Appl. Mater. Interfaces* **2023**, *15*, 15839-15847.

[4] Rajput, M.; Mallik, S. K.; Chatterjee, S.; Shukla, A.; Hwang, S.; Sahoo, S.; Kumar, G. V. P.; Rahman, A. Defect-engineered monolayer MoS$_2$ with enhanced memristive and synaptic functionality for neuromorphic computing. *Commun. Mater.* **2024**, *5*.

[5] Xiong, X.; Wu, F.; Ouyang, Y.; Liu, Y.; Wang, Z.; Tian, H.; Dong, M. Oxygen Incorporated MoS$_2$ for Rectification‐Mediated Resistive Switching and Artificial Neural Network. *Adv. Funct. Mater.* **2024**, *34*.

[6] Liu, L.; Gao, P.; Zhang, M.; Dou, J.; Liu, C.; Shi, T.; Huang, H.; Wang, C.; He, H.; Chen, Z.; Chai, Y.; Wang, J.; Zou, X.; Liao, L.; Wang, J.; Zhou, P. Two‐dimensional MoS$_2$ ‐based anisotropic synaptic transistor for neuromorphic computing by localized electron beam irradiation. *Adv. Sci.* **2024**, *11*, 2408210.

[7] Oh, J.; Park, S.; Lee, S. H.; Kim, S.; Lee, H.; Lee, C.; Hong, W.; Cha, J. H.; Kang, M.; Jin, J. H.; Im, S. G.; Kim, M. J.; Choi, S. Y. Ultrathin all‐solid‐state MoS$_2$ ‐based electrolyte gated synaptic transistor with tunable organic–inorganic hybrid film. *Adv. Sci.* **2024**, *11*, 2308847.

[8] Xu, H.; Sun, F.; Li, E.; Guo, W.; Hua, L.; Wang, R.; Li, W.; Chu, J.; Liu, W.; Luo, J.; Sun, Z. Ferroelectric perovskite/MoS$_2$ channel heterojunctions for wide‐window nonvolatile memory and neuromorphic computing. *Adv. Mater.* **2025**, *37*, 2414339.

[9] Yadav, S.; Patel, C.; Rajbhar, M. K.; Dubey, M.; Kumbhar, D. D.; Dongale, T. D.; Khandelwal, V.; Yuvaraja, S.; Li, X.; Mukherjee, S. Ultralow powered 2D MoS$_2$ -based memristive crossbar array for synaptic applications. *ACS Appl. Mater. Interfaces* **2025**, *17*, 26871-26880.

[10] Liu, G.; Liu, H.; Fan, F.; Gu, Y.; Wei, L.; Xiang, X.; Wang, Y.; Li, Q. MoS$_2$-based quantum dot artificial synapses for neuromorphic computing. *Mater. Today Phys.* **2025**, *53*, 101703.

[11] Ai, T.; Yang, Y.; Lu, J.; Yang, X.; Pei, Z.; Xu, Z.; Song, T.; Zhu, W.; He, S.; Luo, Y. Synergistically constructing dual oxygen/sulfur vacancies and activating lattice oxygen in MoS$_2$/TiO$_2$ via heterointerface charge transfer for catalytic degradation of sulfur-containing VOCs. *Chem. Eng. J.* **2025**, *507*, 160574.